



# The Effect of Aging on the Delamination Fracture Energy of Glass Solar Reflectors

Xin He, Robert Tirawat, and Ross E. Larsen  
*National Renewable Energy Laboratory*

**NREL is a national laboratory of the U.S. Department of Energy  
Office of Energy Efficiency & Renewable Energy  
Operated by the Alliance for Sustainable Energy, LLC**

This report is available at no cost from the National Renewable Energy Laboratory (NREL) at [www.nrel.gov/publications](http://www.nrel.gov/publications).

**Technical Report**  
NREL/TP-2C00-72309  
September 2018

Contract No. DE-AC36-08GO28308

# The Effect of Aging on the Delamination Fracture Energy of Glass Solar Reflectors

Xin He, Robert Tirawat, and Ross E. Larsen  
*National Renewable Energy Laboratory*

## Suggested Citation

He, Xin, Tirawat, Robert, and Ross E. Larsen. 2018. *The Effect of Aging on the Delamination Fracture Energy of Glass Solar Reflectors*. Golden, CO: National Renewable Energy Laboratory. NREL/TP-2C00-72309. <https://www.nrel.gov/docs/fy18osti/72309.pdf>.

**NREL is a national laboratory of the U.S. Department of Energy  
Office of Energy Efficiency & Renewable Energy  
Operated by the Alliance for Sustainable Energy, LLC**

This report is available at no cost from the National Renewable Energy Laboratory (NREL) at [www.nrel.gov/publications](http://www.nrel.gov/publications).

National Renewable Energy Laboratory  
15013 Denver West Parkway  
Golden, CO 80401  
303-275-3000 • [www.nrel.gov](http://www.nrel.gov)

**Technical Report**  
NREL/TP-2C00-72309  
September 2018

Contract No. DE-AC36-08GO28308

## NOTICE

This work was authored by the National Renewable Energy Laboratory, operated by Alliance for Sustainable Energy, LLC, for the U.S. Department of Energy (DOE) under Contract No. DE-AC36-08GO28308. Funding provided by the U.S. Department of Energy Office of Energy Efficiency and Renewable Energy Solar Energy Technologies Office. The views expressed in the article do not necessarily represent the views of the DOE or the U.S. Government.

This report is available at no cost from the National Renewable Energy Laboratory (NREL) at [www.nrel.gov/publications](http://www.nrel.gov/publications).

U.S. Department of Energy (DOE) reports produced after 1991 and a growing number of pre-1991 documents are available free via [www.osti.gov](http://www.osti.gov).

*Cover Photos by Dennis Schroeder: (left to right) NREL 26173, NREL 18302, NREL 19758, NREL 29642, NREL 19795.*

NREL prints on paper that contains recycled content.

# Table of Contents

<b>1</b>	<b>Introduction</b> .....	<b>2</b>
1.1	Accelerated Aging Test for Solar Reflectors.....	3
1.2	Delamination Fracture Energy Testing .....	3
<b>2</b>	<b>Width-Tapered Beam Tests</b> .....	<b>5</b>
2.1	Sample Preparation .....	5
2.2	Data Analysis .....	6
2.3	Testing Results of Unaged Samples .....	8
<b>3</b>	<b>Verification using FE Simulations</b> .....	<b>10</b>
3.1	Determination of Parameters for Cohesive Elements .....	10
3.2	FE Model.....	11
3.3	Simulation Results.....	12
<b>4</b>	<b>Effects of Aging on DFE</b> .....	<b>13</b>
4.1	Accelerated Aging of Oxide-Coated Front-Surfaced Reflectors.....	13
4.2	Testing Results .....	13
<b>5</b>	<b>Conclusions</b> .....	<b>17</b>
	<b>Acknowledgments</b> .....	<b>17</b>
	<b>References</b> .....	<b>18</b>

# List of Figures

Figure 1. Schematic glass reflector designs (Zhang et al., 2016).....	2
Figure 2. Schematic of a width-tapered single cantilever beam sample. The sample is loaded via the tab placed at the apex of its beam as discussed in reference (Bosco et al., 2016). .....	4
Figure 3. Dimensions of the width-tapered acrylic beam with an included angle $\theta = 20^\circ$ and thickness 1.8 mm (Bosco et al., 2016). .....	5
Figure 4. (a) Test configuration, and (b) peeled sample. ....	7
Figure 5. Tested load-displacement curve. ....	7
Figure 6. (a) Two beams glued on each sample, and (b) crack tips after three pulls. ....	7
Figure 7. Bilinear traction-separation response of the cohesive element (Song et al., 2008). ....	10
Figure 8. (a) Mesh of the FE model (b) Boundary conditions of the FE model. ....	11
Figure 9. FE simulation results: (a) Deformation of the sample; (b) Stress field in the metal and cohesive layers. ....	12
Figure 10. Comparison between simulated and tested delamination force.....	12
Figure 11. Plot of the mean of measured DFE after different aging periods with SDM error bar for samples with: (a) $Al_2O_3$ protective coating; and (b) $TiO_2$ protective coating.....	15
Figure A.1. Schematic loaded cantilever beam.....	23
Figure B.1. First-pull load displacement curves for sample 1/beam 1 unaged $Al_2O_3$ -coated (left) and $TiO_2$ -coated (right) reflectors. ....	24
Figure B.2. Second-pull load displacement curves for sample 1/beam 1 unaged $Al_2O_3$ -coated (left) and $TiO_2$ -coated (right) reflectors. ....	24
Figure B.3. Third-pull load displacement curves for sample 1/beam 1 unaged $Al_2O_3$ -coated (left) and $TiO_2$ -coated (right) reflectors. ....	25
Figure B.4. First-pull load displacement curves for sample 1/beam 2 unaged $Al_2O_3$ -coated (left) and $TiO_2$ -coated (right) reflectors. ....	25
Figure B.5. Second-pull load displacement curves for sample 1/beam 2 unaged $Al_2O_3$ -coated (left) and $TiO_2$ -coated (right) reflectors. ....	25
Figure B.6. Third-pull load displacement curves for sample 1/beam 2 unaged $Al_2O_3$ -coated (left) and $TiO_2$ -coated (right) reflectors. ....	26
Figure B.7. First-pull load displacement curves for sample 2/beam 1 unaged $Al_2O_3$ -coated (left) and $TiO_2$ -coated (right) reflectors. ....	26
Figure B.8. Second-pull load displacement curves for sample 2/beam 1 unaged $Al_2O_3$ -coated (left) and $TiO_2$ -coated (right) reflectors. ....	26
Figure B.9. Third-pull load displacement curves for sample 2/beam 1 unaged $Al_2O_3$ -coated (left) and $TiO_2$ -coated (right) reflectors. ....	27
Figure B.10. First-pull load displacement curves for sample 2/beam 2 unaged $Al_2O_3$ -coated (left) and $TiO_2$ -coated (right) reflectors. ....	27
Figure B.11. Second-pull load displacement curves for sample 2/beam 2 unaged $Al_2O_3$ -coated (left) and $TiO_2$ -coated (right) reflectors. ....	27
Figure B.12. Third-pull load displacement curves for sample 2/beam 2 unaged $Al_2O_3$ -coated (left) and $TiO_2$ -coated (right) reflectors. ....	28
Figure B.13. First-pull load displacement curves for sample 1/beam 1 $Al_2O_3$ -coated (left) and $TiO_2$ -coated (right) reflectors aged 50 hours.....	28
Figure B.14. Second-pull load displacement curves for sample 1/beam 1 $Al_2O_3$ -coated (left) and $TiO_2$ -coated (right) reflectors aged 50 hours.....	28
Figure B.15. Third-pull load displacement curves for sample 1/beam 1 $Al_2O_3$ -coated (left) and $TiO_2$ -coated (right) reflectors aged 50 hours.....	29
Figure B.16. First-pull load displacement curves for sample 1/beam 2 $Al_2O_3$ -coated (left) and $TiO_2$ -coated (right) reflectors aged 50 hours.....	29

Figure B.17. Second-pull load displacement curves for sample 1/beam 2 $Al_2O_3$ -coated (left) and $TiO_2$ -coated (right) reflectors aged 50 hours.....	29
Figure B.18. Third-pull load displacement curves for sample 1/beam 2 $Al_2O_3$ -coated (left) and $TiO_2$ -coated (right) reflectors aged 50 hours.....	30
Figure B.19. First-pull load displacement curves for sample 2/beam 1 $Al_2O_3$ -coated (left) and $TiO_2$ -coated (right) reflectors aged 50 hours.....	30
Figure B.20. Second-pull load displacement curves for sample 2/beam 1 $Al_2O_3$ -coated (left) and $TiO_2$ -coated (right) reflectors aged 50 hours.....	30
Figure B.21. Third-pull load displacement curves for sample 2/beam 1 $Al_2O_3$ -coated (left) and $TiO_2$ -coated (right) reflectors aged 50 hours.....	31
Figure B.22. First-pull load displacement curves for sample 2/beam 2 $Al_2O_3$ -coated (left) and $TiO_2$ -coated (right) reflectors aged 50 hours.....	31
Figure B.23. Second-pull load displacement curves for sample 2/beam 2 $Al_2O_3$ -coated (left) and $TiO_2$ -coated (right) reflectors aged 50 hours.....	31
Figure B.24. Third-pull load displacement curves for sample 2/beam 2 $Al_2O_3$ -coated (left) and $TiO_2$ -coated (right) reflectors aged 50 hours.....	32
Figure B.25. First-pull load displacement curves for sample 1/beam 1 $Al_2O_3$ -coated (left) and $TiO_2$ -coated (right) reflectors aged 100 hours.....	32
Figure B.26. Second-pull load displacement curves for sample 1/beam 1 $Al_2O_3$ -coated (left) and $TiO_2$ -coated (right) reflectors aged 100 hours.....	32
Figure B.27. Third-pull load displacement curves for sample 1/beam 1 $Al_2O_3$ -coated (left) and $TiO_2$ -coated (right) reflectors aged 100 hours.....	33
Figure B.28. First-pull load displacement curves for sample 1/beam 2 $Al_2O_3$ -coated (left) and $TiO_2$ -coated (right) reflectors aged 100 hours.....	33
Figure B.29. Second-pull load displacement curves for sample 1/beam 2 $Al_2O_3$ -coated (left) and $TiO_2$ -coated (right) reflectors aged 100 hours.....	33
Figure B.30. Third-pull load displacement curves for sample 1/beam 2 $Al_2O_3$ -coated (left) and $TiO_2$ -coated (right) reflectors aged 100 hours.....	34
Figure B.31. First-pull load displacement curves for sample 2/beam 1 $Al_2O_3$ -coated (left) and $TiO_2$ -coated (right) reflectors aged 100 hours.....	34
Figure B.32. Second-pull load displacement curves for sample 2/beam 1 $Al_2O_3$ -coated (left) and $TiO_2$ -coated (right) reflectors aged 100 hours.....	34
Figure B.33. Third-pull load displacement curves for sample 2/beam 1 $Al_2O_3$ -coated (left) and $TiO_2$ -coated (right) reflectors aged 100 hours.....	35
Figure B.34. First-pull load displacement curves for sample 2/beam 2 $Al_2O_3$ -coated (left) and $TiO_2$ -coated (right) reflectors aged 100 hours.....	35
Figure B.35. Second-pull load displacement curves for sample 2/beam 2 $Al_2O_3$ -coated (left) and $TiO_2$ -coated (right) reflectors aged 100 hours.....	35
Figure B.36. Third-pull load displacement curves for sample 2/beam 2 $Al_2O_3$ -coated (left) and $TiO_2$ -coated (right) reflectors aged 100 hours.....	36

## List of Tables

Table 1. Measured DFE for unaged glass reflectors.....	8
Table 2. Statistical properties of the measured DFE of unaged reflectors.....	9
Table 3. Thickness and Material Properties of Each Layer.....	11
Table 4. Accelerated exposure conditions.....	13
Table 5. Tested DFE for glass reflector 50 hours of aging.....	15
Table 6. Tested DFE for glass reflector 100 hours of aging.....	16
Table 7. Statistical analysis of DFE results for samples with $Al_2O_3$ protective coating.....	16
Table 8. Statistical analysis of DFE results for samples with $TiO_2$ protective coating.....	16

## Abstract

Thin metal and metal oxide films deposited on glass or polymer substrates have been widely applied to manufacture front surfaced solar reflectors such as those used in the concentrated solar power (CSP) systems due to the facts that they are highly transparent, resistant to ultraviolet (UV) light and abrasion, and chemically inert. However, the reliable operation over long periods of outdoor exposure of such solar reflectors depends on the adequate adhesion between each layer to prevent delamination and subsequent failure. We report results from measurements of the delamination fracture energy (DFE) of the weakest interface in both as-deposited and aged reflectors, where the reflector construction consists of a glass/copper/silver/oxide stack. In this study, the DFE was measured using a width-tapered beam method and the test results showed that the weakest interface of this solar reflector is the copper-glass interface, with a DFE of approximately  $4.4 \text{ J/m}^2$ . In order to verify the test results, finite element (FE) simulations were run using the commercial software package ABAQUS 6.14 based on the cohesive zone model (CZM). In the simulations, the DFE derived from the delamination measurement was treated as an input and the delamination forces from the FE simulations were compared to the experimental results. The good agreement between the tested and simulated delamination force indicated that this width-tapered beam method is accurate even for very small DFE, making it appropriate to test the DFE of front surfaced glass solar reflectors. Additionally, in order to study the aging effect on the DFE, accelerated aging tests were conducted using samples with different protective coatings, one group of samples with alumina ( $\text{Al}_2\text{O}_3$ ) protective coating and the other group with titania ( $\text{TiO}_2$ ) protective coating. The DFE after 50 and 100 hours of accelerated aging were measured. The test results showed that the copper-glass interface would still be the weakest interface for all samples after aging, and the DFE for samples with  $\text{Al}_2\text{O}_3$  protective coating was unchanged whereas the copper-glass interface was found to undergo statistically significant change after both 50 and 100 hours of aging for samples with  $\text{TiO}_2$  protective coating. We found that DFE at the copper/glass interface decreased after 50 hours of aging then increased after 100 hours of aging. The origin of this non-monotonic response of  $\text{TiO}_2$  coated reflectors under accelerated aging conditions is unknown.

# 1 Introduction

The reflectors used in concentrated solar power (CSP) systems can be of various constructions, including traditional rear-surfaced glass mirrors (Price et al., 2002), coated aluminum mirrors (Fernández-García et al., 2017) and front surfaced silver mirrors on a variety of substrates (Wilson, 2013). Each type of reflector also can be produced from various materials, such as glass or polymer as substrate, copper layers to act as adhesion promoters between silver and a substrate, silver to reflect the light and coatings such as silica, alumina or titania for reflectance tuning and protective purposes. Currently, most large CSP plants use reflectors with glass support because it is highly transparent, resistant to ultraviolet (UV) light and abrasion, and chemically inert (Edfouf et al., 2015). Figure 1 shows a schematic front-surfaced glass reflector with a bonding layer between the silver and glass, and a protective layer atop the silver. The solar reflectors are important components in the CSP system because the ability to direct light to a target for heating directly impacts the operation efficiency of CSP plants. The large cost associated with construction of the solar field of mirrors means that reflector lifetime, weight and cost must be optimized to lower the levelized cost of energy of CSP plants (IRENA, 2012). The exposure of solar reflectors to environmental conditions (humidity, dust), high radiation fluxes and elevated temperatures potentially causes stress and degradation due to the diffusion of oxygen and moisture into the system which further lead to loss in reflectance throughout the time (DiGrazia et al., 2012; Fernández-García et al., 2014; Edfouf et al., 2015). As the reflectors are costly and cannot be replaced frequently (Hernández-Moro and Martínez-Duart, 2013), the reflectivity should be maintained as long as possible for any reflector that can be adopted for a CSP plant. Based on these considerations, a good bonding between each layer of the solar reflector is desired in order to slow the aging process down and increase the service life. Hence, in this report we tested the interlayer bonding as a route to understanding reflector degradation that may accompany delamination.

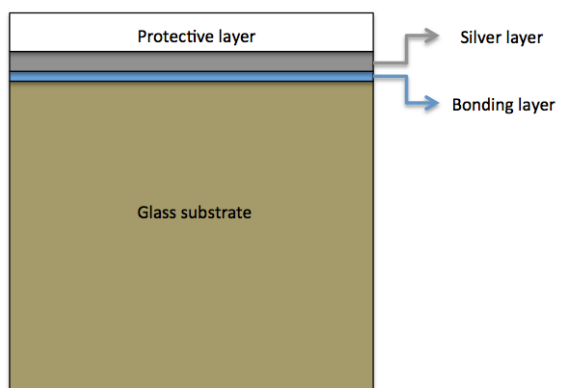


**Figure 1. Schematic glass reflector designs (Zhang et al., 2016).**

In order to quantify the bonding behavior between each layer of front-surfaced glass reflectors and study the effect of aging on the bonding quality, we measured the delamination fracture energy (DFE) at the weakest interface of simplified front-surface reflectors after different periods of accelerated aging. DFE is a material property equal to the energy required to delaminate a unit area of the interface of interest and it is measured using a tapered-beam testing method (Bosco et al., 2016) as described below.

## 1.1 Accelerated Aging Test for Solar Reflectors

Simply aging solar reflectors under ambient conditions does not allow rapid assessment of the durability of solar reflectors because of the multi-year timescale associated with degradation of any reflector of practical interest. The rates and types of degradation also strongly depend on the exposure site and such aging necessarily allows extrinsic damage such as scratching from blown dust. In order to examine intrinsic reflector aging under more controlled conditions, we have performed indoor aging of reflectors with conditions chosen to accelerate aging (Avenel et al., 2017) using an ATLAS MTS Weatherometer, allowing accelerated aging under a concentrated enhanced-UV flux, which gives good correlation with natural aging (Hardcastle et al., 2010). There are many standard accelerated aging test methods that quantitatively evaluate the degradation behavior of glass solar reflectors. Sutter et al. (2014) gives an extensive review of the state of the art of currently applied accelerated aging tests. The testing conditions of relevant tests are summarized and the most widely used accelerated aging tests for reflectors are briefly described. Later, Sutter et al. (2015) performed an extensive test campaign of accelerated aging tests with silvered-glass mirrors from several manufacturers and concluded that accelerated aging testing of samples that showed degradation outdoors and of samples that are outdoor-proven is a good method of checking the effectiveness of the accelerated test methods. Avenel et al. (2017) compared three accelerated aging chambers with different lamps and irradiance levels using five kinds of solar mirrors to establish a standard for CSP mirrors' accelerated aging tests. The results showed that UV5X chamber allowed obtaining degradation similar to that produced in the two other devices, with a reduced time of aging because of higher temperature and humidity than is found outdoors.

## 1.2 Delamination Fracture Energy Testing

There are many testing methods available to measure the DFE of a multi-layered structure: the delamination test which is one of the most frequently used test methods for assessing the failure of flexible laminates, such as those employed in the packaging and electronic industries (Mittal, 1976; Kinloch et al., 1994; Moore and Williams, 2000; Oreski and Wallner, 2005; Jesdinszki et al., 2012; Kucukpinar et al., 2014; Jang et al., 2017); the micro-scratch test which is widely used to assess the adherence of thin film to substrate since it is relatively simple to use and provides simple and rapid qualitative (and semi-quantitative) information (Laugier, 1984; Liu et al., 2004; Rats et al., 1999; Venkataraman et al., 1993); the blister test which relates the pressure at which debond initiates to the work of adhesion of the film (Dannenberg, 1961; Gent and Lewandowski, 1987; Hinkley, 1983; Mittal and Kern, 1987; Allen and Senturia, 1988); the residual-stress driven delamination or micro-strip test developed by Bagchi et al. (1994); the indent test measuring the delamination of ductile coatings on brittle substrates by using a micro-indenter to deform the coating (Evans and Hutchinson, 1984; Rossington et al., 1984; Allen and Senturia, 1988; Drory et al., 1994; Drory and Hutchinson, 1996); the edge peel test during which the fracture process is largely elastic (Drory et al., 1988; Shaffer et al., 1993; Bagchi et al., 1994; Shaffer et al., 1994; McGarry and Shaffer, 1994; Shaffer et al., 1996, 1998); the method based on buckling (Bordet et al., 1998; Hutchinson and Suo, 1991) or crack formation (Omiya and Kishimoto, 2006).

In this study, the DFE of glass reflectors was measured using the with-tapered beam method developed by Bosco et al. (2016). This method employs an elastic, width-tapered cantilever beam adhered to the top surface of the multi-layer structure, see Figure 2. When the beam is loaded at its apex, delamination will initiate at the weakest interface and advance upon continued loading.

The advantage of this method is that the differential of compliance and the width of this width-tapered cantilever beam would increase proportionally with the increase of crack length, therefore the delamination force becomes constant once delamination has been initiated.

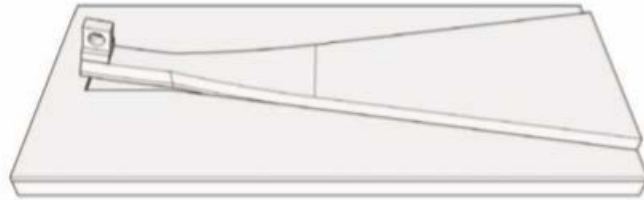


**Figure 2. Schematic of a width-tapered single cantilever beam sample. The sample is loaded via the tab placed at the apex of its beam as discussed in reference (Bosco et al., 2016).**

In the following, Section 2 presents the width-tapered beam test procedures and the measured DFE of original glass reflectors with either alumina ( $Al_2O_3$ ) or titania ( $TiO_2$ ) protective coatings. Section 3 verifies the testing results presented in Section 2 by comparing the tested results to finite element (FE) simulation results based on a cohesive zone model (CZM) of delamination. The results of accelerated aging tests and studies about the effect of aging on DFE are given in Section 4. Finally, some conclusions will be given in section 5.

## 2 Width-Tapered Beam Tests

In this study, the reflectors were prepared by depositing a thin (10 nm) copper layer onto standard, 1/8-in plate glass (green glass) to act as an adhesion layer between glass and a 100-nm layer of silver that acts as the solar reflector. Prior to deposition, the glass was cleaned with pumice, isopropyl alcohol, and a detergent solution (Billco #013-701). The silver reflective layer is coated with 200 nm of either  $Al_2O_3$  or  $TiO_2$  as a protective layer. All layers were deposited with e-beam evaporation and the base pressure of the chamber was on the order of  $3.0 \times 10^{-8}$  torr. The copper was deposited at a rate of  $3.0 \text{ \AA/s}$  from 99.999% copper source material; the silver was deposited at  $5.0 \text{ \AA/s}$  from 99.99% pure source material; the  $TiO_2$  was evaporated from  $Ti_3O_5$  source material (99.9%) at  $5.0 \text{ \AA/s}$  with an oxygen ( $O_2$ ) flow of 10 sccm; and the  $Al_2O_3$  was evaporated from  $Al_2O_3$  source material (99.99%) at  $5.0 \text{ \AA/s}$  with an  $O_2$  flow of 10 standard cubic centimeters per minute (sccm). Layers were deposited sequentially without removing the substrate from vacuum.

Based on the testing results, the DFE of this glass reflector is small, less than  $10 \text{ J/m}^2$ , so a flexible beam is required to allow continuous growth of the crack. (Too stiff a beam can lead to sudden failure rather than a gradual delamination.) Hence, we used a 1.8 mm thick acrylic beam with dimensions given in Figure 3. This beam was glued on the oxide top surface of the glass reflectors and pulled up by a small load frame, with the delamination force continuously monitored. A handle was incorporated into the acrylic beam to provide a location for the attachment of a loading tab whose action could remain at the apex of the beam.

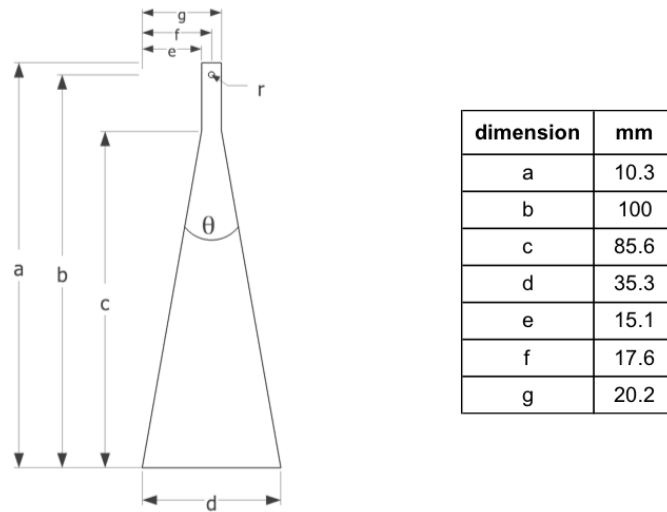


Figure 3. Dimensions of the width-tapered acrylic beam with an included angle  $\theta = 20^\circ$  and thickness 1.8 mm (Bosco et al., 2016).

### 2.1 Sample Preparation

In order to glue the acrylic beam to the glass reflector well, the acrylic beam was roughened using sandpaper. Then the roughened beam surface and the top surface of reflector were cleaned using isopropyl alcohol. After that, a volume of Epoxy (3M-8010) adequate to just cover the tapered acrylic beam was applied to its roughened surface. The acrylic beam was then pressed to the

protective layer of the glass reflectors and held secure for several seconds until the adhesive fully hardened. A sharp razor blade was then used to cut through the metal and metal oxide layers around the acrylic beam using the straight edge of the beam as a guide and a pre-crack was made using a sharp blade.

After the samples were prepared, a small load tab was attached to the handle at the apex of the acrylic beam and connected to the tensile machine. Then the test was conducted at a constant displacement rate of 10  $\mu\text{m/s}$ , the load and load-line displacement were recorded. The test configuration is presented in Figure 4(a). After testing, the sample was unloaded and removed from the loading frame. The crack tip was marked, and the crack length was measured using a caliper. Figure 4(b) presents one tested sample with  $\text{Al}_2\text{O}_3$  protective coating and shows that the delaminated interface is the interface between the copper layer and glass, which denotes that the copper-glass interface is the weakest interface. Figure 5 presents the corresponding load-displacement curve which includes the unloading process.

## 2.2 Data Analysis

For this width-tapered cantilever beam method, the material property of interest, the DFE, is related to the measured parameters as described by Bosco et al. (2016):

$$G_c = \frac{P_c^2}{2b} \frac{dC}{da} \quad (1)$$

where  $P_c$  is the critical load to extend the debonding line,  $b$  is the width of the beam at crack tip, and  $dC/da$  is the derivative of compliance to crack length. Applying the beam theory for this cantilever beam, Eq. (1) can be written as:

$$G_c = \frac{P_c}{2 \tan(\theta/2)} \frac{\Delta_i}{a_i^2} \quad (2)$$

where  $a_i$  is the crack length under a load-line displacement  $\Delta_i$ , and  $\theta$  is the apex angle of the width-tapered beam. From Eq. (2), the DFE can be calculated based on the tested delamination force and the measured crack length with a load-line displacement. For completeness, the details of the derivation of Eqs. (1) and (2) can be found in Appendix A.

Based on the load-displacement curve as shown in Figure 5, the delamination force is not perfectly constant in practice. In order to estimate an average DFE, the DFE at every point in the section where the force is approximately constant (section between the two red dash lines, where the load-line displacement is between 2 mm and 4.4 mm, for the test shown in Fig. 5) was calculated using Eq. (2) based on the measured final crack length and the corresponding delamination force and load-line displacement. Then, the average value was used to represent the DFE of this sample. For this specific sample, the calculated averaged DFE is  $3.9 \text{ J/m}^2$ , and the standard deviation (SD) is  $0.26 \text{ J/m}^2$ .



(a)



(b)

**Figure 4. (a) Test configuration, and (b) peeled sample.**

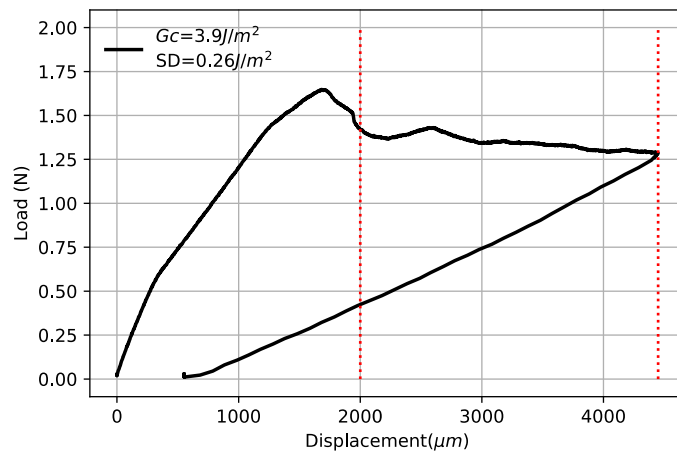
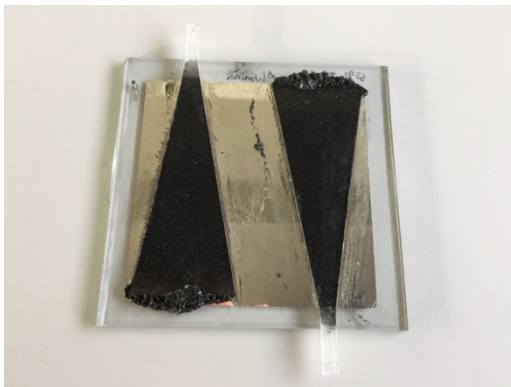


**Figure 5. Tested load-displacement curve.**



(a)



(b)

**Figure 6. (a) Two beams glued on each sample, and (b) crack tips after three pulls.**

## 2.3 Testing Results of Unaged Samples

The tested DFEs for samples with either  $Al_2O_3$  or  $TiO_2$  protective coating are summarized in Table 1. For each type of protective coating, 2 samples were prepared, and 2 beams were glued on each sample as shown in Figure 6(a). In order to investigate the DFE at different locations, 3 pulls were conducted for each beam, the marked crack tips for each beam were shown in Figure 6(b) (the marker closest to the apex of the beam indicates the pre-crack tip). Therefore, 6 DFE values can be obtained for each sample. The samples in the Table 1 are named as follows:  $Al_2O_3$  or  $TiO_2$  indicates the type of protective coating of sample; the following number denotes the first or second sample with same type of protective coating; the second number denotes the first or second beam glued on this sample; and the last number denotes the pull number for this beam. For example, sample  $Al_2O_3$ -1-1-2 denotes the second pull on the first beam on the first alumina-coated reflector. All of the measured load-displacement curves for the unaged samples are included in Appendix B in the panels of Figures B.1-B12.

The measured DFEs for samples with  $Al_2O_3$  protective coating appear on average to be lower than the DFEs of samples with  $TiO_2$  protective coating (as shown in Table 2, the average DFE of samples with  $Al_2O_3$  is  $4.0 \text{ J/m}^2$  which is lower than the average DFE of samples with  $TiO_2$  ( $4.9 \text{ J/m}^2$ )). Table 2 also shows that DFEs for all samples have a large uncertainty. The measured DFEs for samples with  $Al_2O_3$  protective coating range from  $2.6$  to  $5.9 \text{ J/m}^2$ , with a SD of  $1.2 \text{ J/m}^2$ , and from  $3.1$  to  $6.9 \text{ J/m}^2$ , with a SD of  $1.5 \text{ J/m}^2$  for samples with  $TiO_2$  protective coating. The large heterogeneity found in the DFE values indicates that, despite the identical cleaning and deposition procedures, the binding between copper and glass is not uniform over length scales of several mm or cm. The lower SD and standard deviation of the mean (SDM) for samples with  $Al_2O_3$  coating suggests that perhaps the Cu/glass interface in this kind of sample is more uniform compared with samples with  $TiO_2$  coating, but are these apparent differences in mean DFE and in uniformity statistically significant?

**Table 1. Measured DFE for unaged glass reflectors.**

Sample label	DFE ( $\text{J/m}^2$ )	Samples	DFE ( $\text{J/m}^2$ )
$Al_2O_3$ -1-1-1	5.9	$TiO_2$ -1-1-1	6.0
$Al_2O_3$ -1-1-2	5.5	$TiO_2$ -1-1-2	3.3
$Al_2O_3$ -1-1-3	5.6	$TiO_2$ -1-1-3	6.8
$Al_2O_3$ -1-2-1	3.1	$TiO_2$ -1-2-1	6.8
$Al_2O_3$ -1-2-2	2.6	$TiO_2$ -1-2-2	6.9
$Al_2O_3$ -1-2-3	3.2	$TiO_2$ -1-2-3	3.5
$Al_2O_3$ -2-1-1	3.1	$TiO_2$ -2-1-1	5.4
$Al_2O_3$ -2-1-2	2.6	$TiO_2$ -2-1-2	5.6
$Al_2O_3$ -2-1-3	3.4	$TiO_2$ -2-1-3	4.1
$Al_2O_3$ -2-2-1	3.9	$TiO_2$ -2-2-1	3.8
$Al_2O_3$ -2-2-2	5.1	$TiO_2$ -2-2-2	3.6
$Al_2O_3$ -2-2-3	3.5	$TiO_2$ -2-2-3	3.1

We have performed two-tailed Student's t-tests (with 11 degrees of freedom (DOF)) in order to estimate ranges of DFE for each sample type. The results from the two-tailed t-tests show that, with 95% confidence, the DFE of samples with  $Al_2O_3$  coating would be in the range of 3.2 – 4.7 J/m<sup>2</sup>, while the range for samples with  $TiO_2$  coating would be 4.0–5.8 J/m<sup>2</sup>. In principle, we would expect essentially no difference between DFE for samples with  $Al_2O_3$  and  $TiO_2$  coatings; because the weakest interface is the copper-glass interface, the protective coating would be expected to have little effect on the DFE of the buried copper-glass interface. The observed overlap of the 95% confidence intervals is consistent with this idea. Therefore, for unaged samples we will treat all of the samples as a single set with 23 DOF. For the combined set, the mean value for all samples is 4.4 J/m<sup>2</sup> with a SD of 1.4 J/m<sup>2</sup> and SDM of 0.29 J/m<sup>2</sup>. The two-tailed t-test gives a 95% confidence interval for the DFE of 3.8 – 5.0 J/m<sup>2</sup>.

**Table 2. Statistical properties of the measured DFE of unaged reflectors.**

<b>Protective Coating types</b>	<b>Mean</b>	<b>SD</b>	<b>SDM</b>
<i>Al<sub>2</sub>O<sub>3</sub></i>	4.0	1.2	0.4
<i>TiO<sub>2</sub></i>	4.9	1.5	0.4
<b>Both coatings</b>	4.4	1.4	0.3

### 3 Verification using FE Simulations

In this section, we will verify the experimental test results using FE simulation. The experiments showed that delamination always occurred at the copper-glass interface, so the CZM was used to simulate the delamination by inserting cohesive elements between the copper and glass layers in the reflector stack. The constitutive behavior of the cohesive elements was simulated using the bilinear traction-separation law whose response is shown in Figure 7, where  $K$  is the initial stiffness,  $T$  is the strength,  $G_c$  is the critical DFE,  $\Delta^C$  is the separation when delamination is initiated, and  $\Delta^{fail}$  is the separation at damage. For this bilinear traction-separation law, the initial response of the cohesive elements is assumed to be linear until the damage initiation criterion is met (i.e. the stress reaches the strength  $T$ ). After this point, the stress in cohesive elements would be released linearly until the damage evolution property is reached (i.e. fracture energy release rate is equal to  $G_c$ ), and the cohesive elements would be damaged.

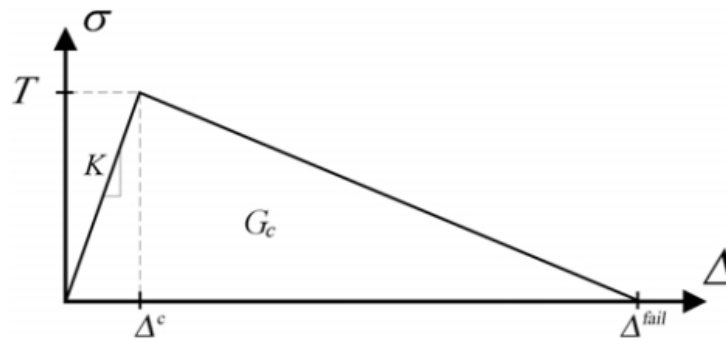


Figure 7. Bilinear traction-separation response of the cohesive element (Song et al., 2008).

#### 3.1 Determination of Parameters for Cohesive Elements

In order to run the simulations, parameters characterizing the bilinear traction-separation law must be specified, including the initial stiffness ( $K$ ), damage initiation threshold ( $T$ ), and damage evolution properties ( $G_c$ ).

As stated before, interface strength determines the damage initiation point; beyond this point damage begins to develop in the cohesive zone leading to reduction in the traction (Saad, 2013). For a bilinear traction-separation law, the interfacial strength can be obtained by applying Eq. (3).

$$T = \frac{2G_c}{\Delta^{fail}} \quad (3)$$

For elastic double cantilever beam analysis, Diehl (2008a) found that a good match with the analytical solution is obtained when  $\Delta^{fail}$  is taken as 0.05 of the cohesive element length.

As for the initial stiffness, Diehl (2005, 2006, 2008a,b) proposed an approach to estimate the elastic stiffness of the cohesive element based on classical fracture mechanics and numerical stability considerations. For a bilinear traction-separation relationship, the stiffness is defined in terms of fracture energy ( $G_c$ ), separation at final failure ( $\Delta^{fail}$ ), and the damage initiation ratio ( $\Delta_{ratio} = \Delta^C/\Delta^{fail}$ ) as:

$$K = \frac{2G_c T_0}{\Delta_{ratio} (\Delta^{fail})^2} \quad (4)$$

Where  $T_0$  is the specified initial constitutive thickness of the cohesive element (typically specified as 1.0 mm). Diehl (2008a) has parametrically studied the effects of  $\Delta_{ratio}$  on various mode I fracture characteristics of elastic double cantilever beam. The results of his parametric studies reveal that  $\Delta_{ratio}$  does not significantly affect the overall load-displacement response of the specimen when compared with the benchmark solution; he recommends a value of 0.5 ( $\Delta_{ratio} = 0.5$ ).

For the damage evolution, the energy criterion was used. Once the fracture energy is higher than the measured DFE ( $3.9 \text{ J/m}^2$ ), the fracture will initiate and propagate.

### 3.2 FE Model

In this study, the simulations were done using the commercial software ABAQUS 6.13 (Simulia, A.V., 2013). The FE model and mesh are shown in Figure 8(a). In total, 16476 uniformly-sized, linear mechanical elements with a size of 1 mm were employed to mesh the structure. In order to simulate the delamination between the copper and glass interface, a layer of cohesive element (COH3D8) was introduced between copper and glass. The thickness of the cohesive layer was 10 nm, and the DFE was  $3.9 \text{ J/m}^2$ . The strength and initial stiffness, obtained based on Eq. (3), (4) and reference (Diehl, 2008a), were 0.157 MPa and 6.29 MPa, respectively. Except for the cohesive layer, all other materials were simulated using C3D8R elements. The thickness and material properties of these layers are summarized in Table 3.

The boundary conditions of the FE model are presented in Figure 8(b), where the bottom of the glass and the widest part of all layers were fixed to ensure the cantilever beam condition. A velocity boundary condition was applied at the hole near the apex to simulate the constant speed pull test.

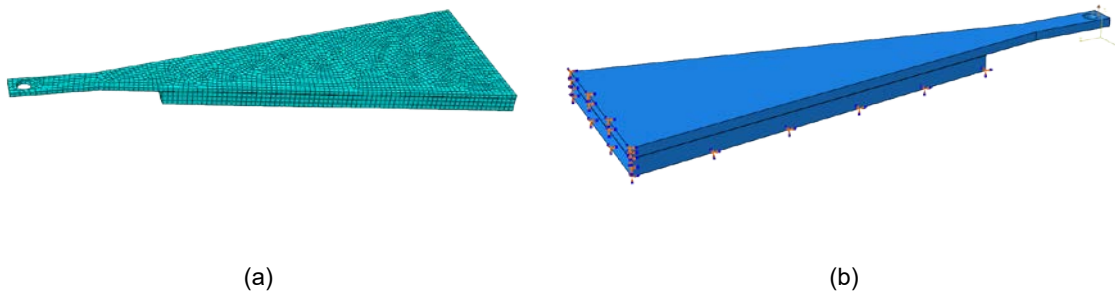


Figure 8. (a) Mesh of the FE model (b) Boundary conditions of the FE model.

Table 3. Thickness and Material Properties of Each Layer.

Layers	Thickness(nm)	Young's Modulus (GPa)	Poisson's Ratio
Acrylic Beam	$1.8 \times 10^6$	3.2	0.35
Glass	$3.175 \times 10^6$	50	0.22
TiO2	200 nm	230	0.27
Ag	100 nm	83	0.37
Cu	10 nm	110	0.34

### 3.3 Simulation Results

The deformed shape and the overall stress field of a simulated delaminated sample are presented in Figure 9(a). The stresses in the beam and glass substrate were much lower compared with that in the metal layer. The reason is that the metal layer is much stiffer than the acrylic beam; therefore, the metal layer would take more stress. In addition, the small DFE prevents the bend of the beam and limits the stress transferred to the glass substrate. The stress distributions in the metal and remaining cohesive layer (blue part) are shown in Figure 9(b). It indicates that the stress in the metal layer is much higher than that in the cohesive layer as the cohesive element can not sustain high load due to the low DFE.

After simulation, the history output of the reaction force at the hole is recorded and compared with the tested delamination force in Figure 10. It shows that the FE simulation can capture the increase of force before delamination and the delamination force is near constant during the delamination process. This is consistent with the theoretical prediction, but the near-constancy is in sharp contrast to the expectation of a constant delamination force after onset of delamination. Figures B.1-B.12 show that, in general, the tested delamination force decreases with the increase of crack length. This could be caused by many factors such as non-uniform bonding across the interface such that the DFE varies with respect to crack length. The consistent *decrease* following onset of failure is consistent with the idea that if there is an initial area near the front of the tapered beam with a larger DFE, this must be delaminated with a large delamination force, but then the growing crack length reduces the probability that there will be an anomalously large DFE averaged over the crack length. Although such an explanation is consistent with our observations, we cannot say with certainty that this is the correct explanation. Further study of such effects with the tapered-beam method are warranted.

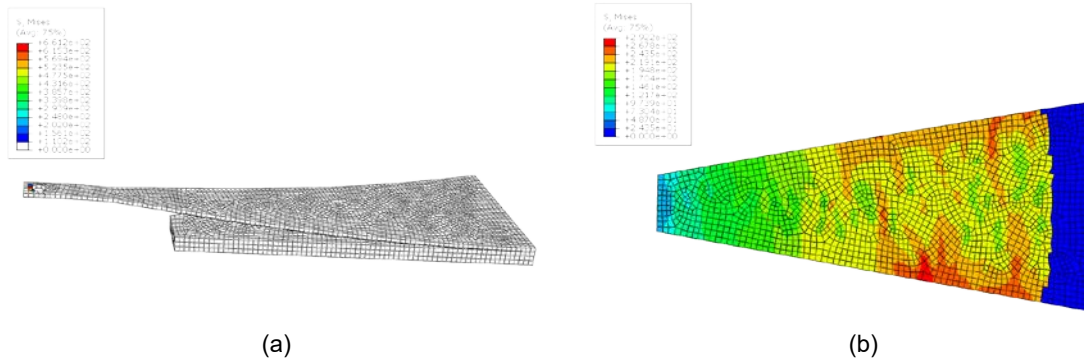


Figure 9. FE simulation results: (a) Deformation of the sample; (b) Stress field in the metal and cohesive layers.

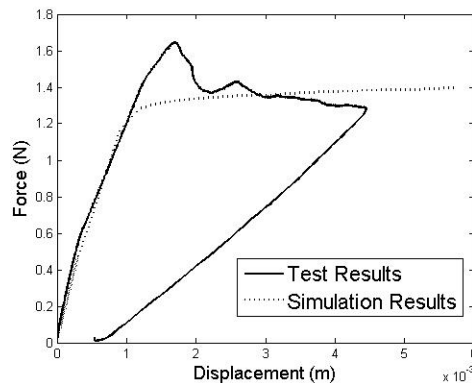


Figure 10. Comparison between simulated and tested delamination force.

## 4 Effects of Aging on DFE

In order to investigate the effect of aging on the bonding of each interface of the glass reflectors, accelerated aging tests were conducted and the DFEs at the weakest interface were measured after 50 and 100 hours of aging using the width-tapered beam method.

### 4.1 Accelerated Aging of Oxide-Coated Front-Surfaced Reflectors

In these tests, customized aging conditions of temperature, humidity and irradiance were applied using an Atlas Ci5000 weatherometer. The Ci5000 is a 12000 W xenon arc lamp environmental chamber with temperature and humidity control. Irradiance from the xenon lamp is filtered to simulate the terrestrial solar spectrum with a Right Light<sup>®</sup> inner filter and a CIRA (coated infrared absorbing) quartz outer filter. Irradiance is controlled to a 340 nm set point. In addition to chamber temperature and humidity control, an uninsulated black panel sensor is used to monitor and control the maximum rack temperature. The exposure conditions used to stress specimens are listed in Table 4.

**Table 4. Accelerated exposure conditions.**

Parameter	Set Point
Irradiance (340 nm)	0.7 W/m <sup>2</sup>
Chamber Temperature	45°C
Relative Humidity	40% RH
Rack Temperature	45°C

To prevent the penetration of oxygen and humidity to the sample through the edge, 3M weather resistant film tape 838 was used to cover the edge of coatings during the accelerated aging tests.

### 4.2 Testing Results

After aging for 50 or 100 hours, the samples were removed from the chamber and the DFE were measured using the width-tapered beam method as described above. The results show that, as for the unaged samples described in Section 2.2, delamination would initiate at the interface of copper and glass for all aged samples, with either  $Al_2O_3$  or  $TiO_2$  protective coating. Hence, the copper-glass interface is still the weakest interface after 50 or 100 hours of aging, indicating that even the photo-reactive  $TiO_2$  remains bonded to silver better than the copper ever is to the glass.

The measured DFEs for all samples after 50 and 100 hours of aging are summarized in Table 5 and 6, respectively. As for the unaged samples, 2 samples were prepared for each type of protective coating for each aging period, 2 beams were glued on each sample, and 3 pulls were conducted for each beam. The samples are named using the same rule as that in Section 3.3. All of the measured load-displacement curves for samples after 50 hours of aging are shown in Figures B.13-B.24 of Appendix B, and the measured load-displacement curves for samples after 100 hours of aging can be found in Figures B.25-B.36.

Results of statistical analysis of the testing results for samples with  $Al_2O_3$  or  $TiO_2$  protective coatings are presented in Tables 7 and 8, respectively. The measured mean DFE after different

aging periods are plotted in Figure 10 with error bars indicating plus or minus one SDM. We can see that after aging there is a large uncertainty for the measured DFE, with a SD higher than  $0.5 \text{ J/m}^2$  for both types of samples after both aging periods, but a smaller SDM than for unaged samples. One interpretation of this reduced uncertainty for aged samples is that the aging causes a kind of annealing that makes the interfacial bonding more uniform. This would imply that the measured force-displacement curves would be less variable in the “constant force” region for aged samples than for unaged samples, and this does not appear to be the case for all samples. Hence, it is not clear what the explanation is for the smaller SDM upon aging.

Two-tailed t-tests were conducted in order to obtain confidence intervals DFE. The obtained 95% confidence intervals are summarized in Tables 7 and 8 and compared with the statistical analysis results for samples without any aging (Recall that for unaged reflectors, samples with different protective coatings were treated as the same for the statistical analysis.)

Based on the statistical analysis, the DFE for samples with  $\text{Al}_2\text{O}_3$  protective coating are found to decrease slightly, but in a non-statistically significant amount upon aging: The mean of DFE decreases by about 8.3% after 50 hours of aging while it decreases by about 11.1% from its initial value after 100 hours aging. In view of the large uncertainty of the measured DFE for all aging conditions, the reduced DFE with aging period is negligible with an  $\text{Al}_2\text{O}_3$  coating. Therefore, we can state that the aging has very minor effect on the DFE of samples with  $\text{Al}_2\text{O}_3$  protective coating. This result is consistent with the finding that the reflector with a protective  $\text{Al}_2\text{O}_3$  coating represents an advancement in solar reflector durability, as samples of the reflector have shown an initial solar-weighted hemispherical reflectance of 95% and outstanding optical performance in both accelerated and outdoor (Colorado) exposure testing (Kennedy et al., 1997).

In contrast to what happens with  $\text{Al}_2\text{O}_3$  protective coating, the DFE for  $\text{TiO}_2$  coated samples shows large and significant changes upon aging. After 50 hours, the mean DFE has decreased more than 30%, with the 95% confidence intervals at 0 and 50 hours of aging not overlapping at all. This suggests that  $\text{TiO}_2$  coatings do not provide sufficient encapsulation to prevent modifications occurring at the Cu/glass interface; this is consistent with the larger changes in reflectance we have found for  $\text{TiO}_2$ -coated reflectors constructed and aged the same way (unpublished results). Mysteriously, for  $\text{TiO}_2$ -coated samples aged for 100 hours, we see a large and statistically significant *increase* in the DFE, to a value twice that of the as-deposited reflectors. It is unclear at this time what mechanism could lead to an initial decrease in DFE and then a subsequent increase for a buried interface that has no direct contact with the coating. Clearly, further studies would be of interest to verify and understand this observation.

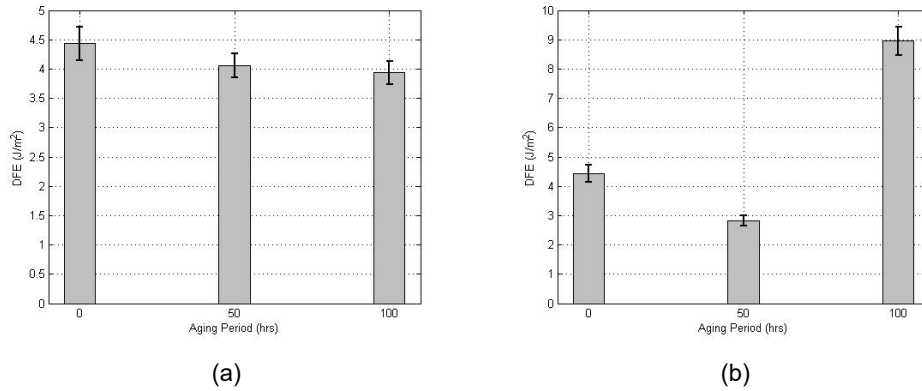


**Figure 11. Plot of the mean of measured DFE after different aging periods with SDM error bar for samples with: (a)  $Al_2O_3$  protective coating; and (b)  $TiO_2$  protective coating.**

**Table 5. Tested DFE for glass reflector 50 hours of aging.**

Samples	DFE ( $J/m^2$ )	Samples	DFE ( $J/m^2$ )
$Al_2O_3$ -1-1-1	4.7	$TiO_2$ -1-1-1	3.5
$Al_2O_3$ -1-1-2	3.8	$TiO_2$ -1-1-2	3.0
$Al_2O_3$ -1-1-3	3.2	$TiO_2$ -1-1-3	3.5
$Al_2O_3$ -1-2-1	2.7	$TiO_2$ -1-2-1	2.5
$Al_2O_3$ -1-2-2	5.0	$TiO_2$ -1-2-2	2.0
$Al_2O_3$ -1-2-3	4.6	$TiO_2$ -1-2-3	2.0
$Al_2O_3$ -2-1-1	4.4	$TiO_2$ -2-1-1	3.2
$Al_2O_3$ -2-1-2	4.4	$TiO_2$ -2-1-2	3.2
$Al_2O_3$ -2-1-3	3.6	$TiO_2$ -2-1-3	3.0
$Al_2O_3$ -2-2-1	4.8	$TiO_2$ -2-2-1	3.3
$Al_2O_3$ -2-2-2	4.1	$TiO_2$ -2-2-2	2.5
$Al_2O_3$ -2-2-3	3.4	$TiO_2$ -2-2-3	2.1

**Table 6. Tested DFE for glass reflector 100 hours of aging.**

Samples	DFE ( $J/m^2$ )	Samples	DFE ( $J/m^2$ )
$Al_2O_3$ -1-1-1	4.8	$TiO_2$ -1-1-1	7.6
$Al_2O_3$ -1-1-2	4.6	$TiO_2$ -1-1-2	7.1
$Al_2O_3$ -1-1-3	5.5	$TiO_2$ -1-1-3	8.1
$Al_2O_3$ -1-2-1	3.4	$TiO_2$ -1-2-1	10.3
$Al_2O_3$ -1-2-2	3.1	$TiO_2$ -1-2-2	12.4
$Al_2O_3$ -1-2-3	3.7	$TiO_2$ -1-2-3	7.6
$Al_2O_3$ -2-1-1	3.6	$TiO_2$ -2-1-1	7.3
$Al_2O_3$ -2-1-2	4.1	$TiO_2$ -2-1-2	9.6
$Al_2O_3$ -2-1-3	3.9	$TiO_2$ -2-1-3	11.1
$Al_2O_3$ -2-2-1	3.6	$TiO_2$ -2-2-1	8.6
$Al_2O_3$ -2-2-2	3.5	$TiO_2$ -2-2-2	8.0
$Al_2O_3$ -2-2-3	3.4	$TiO_2$ -2-2-3	9.8

**Table 7. Statistical analysis of DFE results for samples with  $Al_2O_3$  protective coating.**

Aging period (hours)	Mean	SD	SDM	Range of DFE (95%)
0	4.4	1.4	0.3	[3.8 5.0]
50	4.1	0.7	0.2	[3.6 4.5]
100	3.9	0.7	0.2	[3.5 4.4]

**Table 8. Statistical analysis of DFE results for samples with  $TiO_2$  protective coating.**

Aging period (hours)	Mean	SD	SDM	Range of DFE (95%)
0	4.4	1.4	0.3	[3.8, 5.0]
50	2.8	0.6	0.2	[2.5, 3.2]
100	8.9	1.7	0.5	[7.9, 10.0]

## 5 Conclusions

In this study, the width-tapered single cantilever beam method was applied to test the DFE of the glass reflectors with either  $Al_2O_3$  or  $TiO_2$  protective coating. The DFE measured in our tests showed substantial variation even for different pulls on the same sample, suggesting perhaps that the surface interaction at the Cu/glass interface varies widely at different positions of each sample. In other words, the delaminated interface may not be homogeneous and the DFE would depend on both the crack length and the location of the delaminated region. We found that for both as-deposited and aged reflectors, the copper-glass interface was the weakest. The measured DFE of samples with  $Al_2O_3$  protective coating was slightly lower and with a smaller variance than for samples with  $TiO_2$  protective coating, but unaged samples with both coatings have overlapping confidence intervals. Hence, our statistical analysis of the DFE of unaged reflectors combined the results from both protective coatings. An averaged DFE was obtained as  $4.4 \text{ J/m}^2$  to represent the DFE of original samples.

The results of the tapered-beam pull tests were verified by FE simulation using ABAQUS based on CZM with parameters for cohesive elements obtained based on literature. The delamination force generated from the FE simulation was compared with the test results and it was shown that the simulated delamination force did become nearly constant, with a plateau value that agreed well with the testing results, on average. This good agreement denoted that the width-tapered beam testing method provided an accurate way to measure the DFE of this glass reflector. A decrease of the delamination force following the initial fracture was observed for most tests, suggesting that the wide range of DFE values measured is based on in-sample inhomogeneity, rather than on variations between the different members of our sample sets.

In addition, the effect of aging on the DFE was investigated by measuring the change of DFE in samples after different periods (50 hours or 100 hours) of accelerated aging. The results showed that the DFE of samples with  $Al_2O_3$  protective coating would slightly decrease with the increase of aging period; however, this decrease was within the statistical uncertainty of our data. Therefore, we concluded that the aging had little effect on the DFE of samples with  $Al_2O_3$  samples, and  $Al_2O_3$  coating was a good protective coating. For the samples with  $TiO_2$  protective coating, the DFE was found to decrease after 50 hours of aging but increase after 100 hours of aging. This result was statistically significant but mystifying. In order to understand this strange aging behavior for DFE in samples with  $TiO_2$  protective coating, further studies would seem to be needed.

## Acknowledgments

This work was supported by the U.S. Department of Energy under Contract No. DE-AC36-08-GO28308 with the National Renewable Energy Laboratory through the DOE SETP program. The U.S. Government retains and the publisher, by accepting the article for publication, acknowledges that the U.S. Government retains a nonexclusive, paid-up, irrevocable, worldwide license to publish or reproduce the published form of this work, or allow others to do so, for U.S. Government purposes. We thank Dr. Nick Bosco for helpful discussions and for assistance with the width-tapered cantilever beam measurements.

## References

- Allen, M. G., Senturia, S. D., 1988. Analysis of critical debonding pressures of stressed thin films in the blister test. *The Journal of Adhesion* 25 (4), 303–315.
- Avenel, C., Gardette, J.-L., Therias, S., Disdier, A., Raccurt, O., 2017. Accelerated aging test of solar mirrors: Comparison of different UV chambers. In: *AIP Conference Proceedings*. Vol. 1850. AIP Publishing, p. 130001.
- Bagchi, A., Lucas, G., Suo, Z., Evans, A., 1994. A new procedure for measuring the decohesion energy for thin ductile films on substrates. *Journal of Materials Research* 9 (7), 1734–1741.
- Bordet, H., Ignat, M., Dupeux, M., 1998. Analysis of the mechanical response of film on substrate systems presenting rough interfaces. *Thin Solid Films* 315 (1), 207–213.
- Bosco, N., Tracy, J., Dauskardt, R., Kurtz, S., 2016. Development and first results of the width-tapered beam method for adhesion testing of photovoltaic material systems. In: *Photovoltaic Specialists Conference (PVSC), 2016 IEEE 43rd*. IEEE, pp. 0106–0110.
- Dannenbergh, H., 1961. Measurement of adhesion by a blister method. *Journal of Applied Polymer Science* 5 (14), 125–134.
- Diehl, T., 2005. Modeling surface-bonded structures with ABAQUS cohesive elements: beam-type solutions. In: *ABAQUS User's conference*.
- Diehl, T., 2006. Using ABAQUS cohesive elements to model peeling of an epoxy-bonded aluminum strip: A benchmark study for inelastic peel arms. In: *2006 ABAQUS Users' Conference*.
- Diehl, T., 2008a. On using a penalty-based cohesive-zone finite element approach, part i: Elastic solution benchmarks. *International Journal of Adhesion and Adhesives* 28 (4), 237–255.
- Diehl, T., 2008b. On using a penalty-based cohesive-zone finite element approach, part ii: Inelastic peeling of an epoxy-bonded aluminum strip. *International Journal of Adhesion and Adhesives* 28 (4), 256–265.
- DiGrazia, M., Jorgensen, G., Gee, R., Bingham, C., 2012. Service life prediction for ReflecTech® mirror film. In: *Proceedings of the 41st ASES National Solar Conference 2012 (Solar 2011)*.
- Drory, M., Hutchinson, J., 1996. Measurement of the adhesion of a brittle film on a ductile substrate by indentation. In: *Proceedings of the Royal Society of London A: Mathematical, Physical and Engineering Sciences*. Vol. 452. The Royal Society, pp. 2319–2341.
- Drory, M., Hutchinson, J., et al., 1994. Diamond coating of titanium alloys. *Science-AAAS-Weekly Paper Edition- including Guide to Scientific Information* 263 (5154), 1753–1755.
- Drory, M. D., Thouless, M. D., Evans, A. G., 1988. On the decohesion of residually stressed thin films. *Acta Metallurgica* 36 (8), 2019–2028.

Edfouf, Z., Guerguer, M., Raccurt, O., 2015. Glass and polymeric mirrors ageing under different Moroccan weathers, an application for CSP power plants. *Energy Procedia* 69, 1508–1518.

Evans, A., Hutchinson, J., 1984. On the mechanics of delamination and spalling in compressed films. *International Journal of Solids and Structures* 20 (5), 455–466.

Fernández-García, A., Cantos-Soto, M. E., Röger, M., Wieckert, C., Hutter, C., Martínez-Arcos, L., 2014. Durability of solar reflector materials for secondary concentrators used in CSP systems. *Solar Energy Materials and Solar Cells* 130, 51–63.

Fernández-García, A., Sutter, F., Fernandez-Reche, J., Lüpfert, E., 2017. *The Performance of Concentrated Solar Power (CSP) Systems*. Woodhead Publishing.

Gent, A., Lewandowski, L., 1987. Blow-off pressures for adhering layers. *Journal of Applied Polymer Science* 33 (5), 1567–1577.

Hardcastle, H. K., Jorgensen, G. J., Bingham, C. E., 2010. Ultra-accelerated weathering system i: design and functional considerations. *Journal of Coatings Technology* 7 (NREL/JA-550-49455).

Hernández-Moro, J., Martínez-Duart, J., 2013. Analytical model for solar PV and CSP electricity costs: Present LCOE values and their future evolution. *Renewable and Sustainable Energy Reviews* 20, 119–132.

Hinkley, J., 1983. A blister test for adhesion of polymer films to SiO<sub>2</sub>. *The Journal of Adhesion* 16 (2), 115–125.

Hutchinson, J., Suo, Z., 1991. Mixed mode cracking in layered materials. In: John W. Hutchinson and Theodore Y. Wu (Ed.), *Advances in Applied Mechanics*. Vol. Volume 29. Elsevier, pp. 63–191.

International Renewable Energy Working Paper, *Renewable Energy Technologies: Cost Analysis Series Vol. 1: Power Sector, Issue 2/5, “Concentrating Solar Power”*, 2012

Jang, J., Sung, M., Han, S., Yu, W.R., 2017. Prediction of delamination of steel-polymer composites using cohesive zone model and peeling tests. *Composite Structures* 160, 118–127.

Jesdinszki, M., Struller, C., Rodler, N., Blondin, D., Cassio, V., Kucukpinar, E., Langowski, H.C., 2012. Evaluation of adhesion strength between thin aluminum layer and poly (ethylene terephthalate) substrate by peel tests-a practical approach for the packaging industry. *Journal of Adhesion Science and Technology* 26 (20-21), 2357–2380.

Kennedy, C., Smilgys, R., Kirkpatrick, D., Ross, J., 1997. Optical performance and durability of solar reflectors protected by an alumina coating. *Thin Solid Films* 304 (1-2), 303–309.

Kinloch, A., Lau, C., Williams, J., 1994. The peeling of flexible laminates. *International Journal of Fracture* 66 (1), 45–70.

Kucukpinar, E., Jesdinszki, M., Rodler, N., Struller, C., Noller, K., Blondin, D., Cassio, V., Langowski, H.C., 2014. Determination of metal adhesion strength of metallized films by peel tests. In: Web Coating and Handling Conference.

Laugier, M. T., 1984. An energy approach to the adhesion of coatings using the scratch test. *Thin Solid Films* 117 (4), 243–249.

Liu, Z., Sun, J., Wu, J.-D., Wang, P.-N., Shen, W., 2004. Determination of adhesion energy of CN<sub>x</sub> thin film on silicon from micro-scratch testing. *Tribology Transactions* 47 (1), 130–137.

McGarry, F. J., Shaffer, E. O., 1994. A method for analyzing the critical adhesion energy of thin film coatings. *MRS Online Proceedings Library Archive* 356.

Mittal, K., 1976. Adhesion measurement of thin films. *Active and Passive Electronic Components* 3 (1), 21–42.

Mittal, K., Kern, W., 1987. Selected bibliography on adhesion measurement of films and coatings. *Journal of Adhesion Science and Technology* 1 (1), 247–262.

Moore, D., Williams, J., 2000. The measurement of peel strength and the determination of the interfacial work of fracture for flexible laminates. *European Structural Integrity Society* 27, 231–246.

Omiya, M., Kishimoto, K., 2006. Interfacial strength of ceramic thin film on polymer substrate. In: 16th European Conference of Fracture. Kluwer Academic Publishers.

Oreski, G., Wallner, G., 2005. Delamination behaviour of multi-layer films for PV encapsulation. *Solar energy materials and solar cells* 89 (2), 139–151.

Price, H., Lüpfer, E., Kearney, D., Zarza, E., Cohen, G., Gee, R., Mahoney, R., 2002. Advances in parabolic trough solar power technology. *Journal of solar energy engineering* 124 (2), 109–125.

Rats, D., Hajek, V., Martinu, L., 1999. Micro-scratch analysis and mechanical properties of plasma-deposited silicon-based coatings on polymer substrates. *Thin Solid Films* 340 (1), 33–39.

Rossington, C., Evans, A. G., Marshall, D. B., Khuri-Yakub, B., 1984. Measurements of adherence of residually stressed thin films by indentation. ii. experiments with ZNO/Si. *Journal of Applied Physics* 56 (10), 2639–2644.

Saad, 2013. Selecting material parameters in ABAQUS for cohesive elements defined in terms of traction-separation.

Shaffer, E., McGarry, F., Hoang, L., 1996. Designing reliable polymer coatings. *Polymer Engineering & Science* 36 (18), 2375–2381.

Shaffer, E., Mills, M., Hawn, D., Van Gestel, M., Knorr, A., Gundlach, H., Kumar, K., Kaloyeros, A., Geer, R., 1998. Adhesion energy measurements of multilayer low-K dielectric materials for ULSI applications. *MRS Online Proceedings Library Archive* 511.

Shaffer, E. O., McGarry, F. J., Trusell, F., 1993. Edge delamination testing: A method for measuring the adhesion of thin-film coatings in microelectronic applications part 1: Numerical analysis and preliminary results. MRS Online Proceedings Library Archive 308.

Shaffer, E. O., Sikorski, S. A., McGarry, F. J., 1994. The edge delamination test: Measuring the critical adhesion energy of thin-film coatings, part ii: Mode mixity & application. MRS Online Proceedings Library Archive 338.

Simulia, A.V., 2013. 6.13 Documentation. Dassault systemes.

Song, K., Dávila, C. G., Rose, C. A., 2008. Guidelines and parameter selection for the simulation of progressive delamination. In: ABAQUS Users Conference. Vol. 41. pp. 43–44.

Sutter, F., Fernández-García, A., Heller, P., Anderson, K., Wilson, G., Schmücker, M., Marvig, P., 2015. Durability testing of silvered-glass mirrors. Energy Procedia 69, 1568–1577.

Sutter, F., Fernández-García, A., Wette, J., Heller, P., 2014. Comparison and evaluation of accelerated aging tests for reflectors. Energy Procedia 49, 1718–1727.

Venkataraman, S.K., Nelson, J.C., Hsieh, A.J., Kohlstedt, D.L., Gerberich, W.W., 1993. Continuous microscratch measurements of thin film adhesion strengths. Journal of Adhesion Science and Technology 7 (12), 1279–1292.

Wilson, R.N., 2013. Reflecting telescope optics II: manufacture, testing, alignment, Modern Techniques. Springer Science & Business Media.

Zhang, C., Gray, M.H., Tirawat, R., Larsen, R.E., Chen, F., 2016. The effects of UV aging on the cracking of titanium oxide layer on poly (ethylene terephthalate) substrate.

## Appendix A. Derivation of Delamination Fracture Energy for the Width-tapered Beam Method

Based on the elastic fracture mechanics, the critical delamination fracture energy (DFE) can be written as

$$(DA)G = DW_{ext} - DU \quad (\text{A.1})$$

where  $G_c$  is the critical DFE,  $DA$  is the change of delamination area,  $DW_{ext}$  is the change of total input external work, and  $DU$  is the change of strain energy. Consider an infinitesimal increase of the delamination area, Eq. (A.1) becomes:

$$G_c = \frac{d(W_{ext} - U)}{dA} \quad (\text{A.2})$$

For the elastic structure,

$$W_{ext} = P_c \Delta = 2U \quad (\text{A.3})$$

where  $P_c$  is the delamination force and  $\Delta$  is the load-line displacement. Substituting Eq. (A.3) to (A.2) yields:

$$G_c = \frac{d(P_c \Delta)}{2dA} \quad (\text{A.4})$$

which for constant delamination force can be written as:

$$G_c = P_c \frac{d(\Delta)}{2dA} \quad (\text{A.5})$$

Recall  $P_c = \Delta C$ , where  $C$  is the compliance, so Eq. (A.5) becomes:

$$G_c = \frac{P_c^2}{2} \frac{d(C)}{dA} \quad (\text{A.6})$$

For the width-tapered beam, the delamination area with a crack length of  $a$  can be written as:

$$A = \frac{ba}{2} = a^2 \tan\left(\frac{\theta}{2}\right) \quad (\text{A.7})$$

and

$$dA = d\left(\frac{ba}{2}\right) = 2a \tan\left(\frac{\theta}{2}\right) da = bda \quad (\text{A.8})$$

where  $b$  is the width of the width-tapered beam at the crack tip ( $b = 2a \cdot \tan(\theta/2)$ ). Substituting Eq. (A.8) into (A.6) produces:

$$G_c = \frac{P_c^2}{2} \frac{d(C)}{bda} \quad (\text{A.9})$$

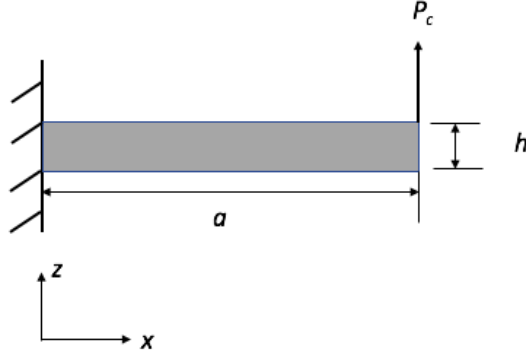


**Figure A.1. Schematic loaded cantilever beam**

To compute  $dC/da$ , the beam theory should be applied. Consider the width-tapered cantilever beam with a length of  $a$ , thickness of  $h$  under a loading of  $P_c$  at one end as shown in Figure A.1, the relationship between bending angle and bending moment is:

$$\beta(x) = \int_0^x \frac{M(X)}{EI} dX \quad (\text{A.10})$$

where  $M(X)$  is the bending moment at  $x$  and it is equal to  $(a-X)P_c$ ,  $E$  is the Young's modulus of the beam, and  $I$  is the moment of inertia which is equal to  $h^3b(X)/12$ . for this beam with rectangular cross section. Here,  $b(X)$  is the width at  $X$ , which is equal to  $2(a - X) \cdot \tan(\theta/2)$  for a tapered beam. Plugging the expression for  $M(X)$ ,  $b(X)$  and  $I$  to Eq. (A.10), one gets:

$$\beta(x) = \int_0^x \frac{12(a - X)P_c}{Eh^3b(X)} dX = \int_0^x \frac{6(a - X)P_c}{Eh^3(a - X)\tan(\theta/2)} dX = \frac{6xP_c}{Eh^3\tan(\theta/2)} \quad (\text{A.11})$$

Consider the relationship between the bending angle and deflection at the end,  $\Delta(x = a) = \int_0^a \beta(x)dx$ , and apply Eq. (A.11), the deflection at the end where the load is applied can be obtained,

$$\Delta(x = a) = \int_0^a \frac{6XP_c}{Eh^3\tan(\theta/2)} dX = \frac{3P_c a^2}{Eh^3\tan(\theta/2)} \quad (\text{A.12})$$

Then the compliance can be written as:

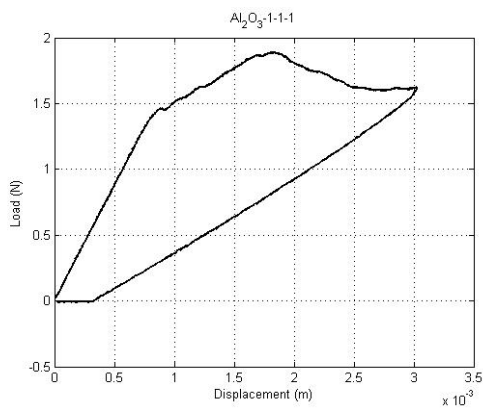
$$C = \frac{\Delta(x = a)}{P_c} = \frac{3a^2}{Eh^3\tan(\theta/2)} \quad (\text{A.13})$$

Applying Eq. (A.13) into Eq. (A.9), the DFE can be expressed as:

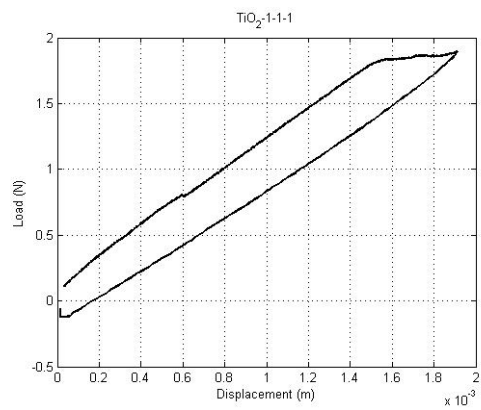
$$G_c = \frac{3P_c^2}{2Eh^3\tan^2(\theta/2)} \quad (\text{A.14})$$

Finally, Eq. (2) can be obtained by combining Eq. (A.12) and (A.14).

## Appendix B. Load-displacement Curves for All Samples

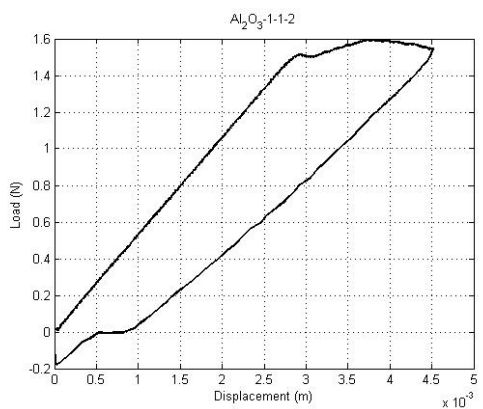


(a) Unaged  $Al_2O_3$  -1-1-1

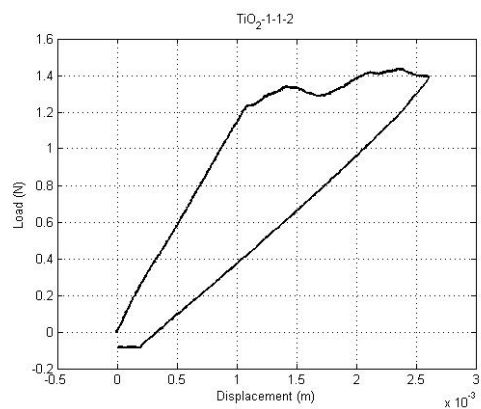


(b) Unaged  $TiO_2$  -1-1-1

**Figure B.1. First-pull load displacement curves for sample 1/beam 1 unaged  $Al_2O_3$ -coated (left) and  $TiO_2$ -coated (right) reflectors.**

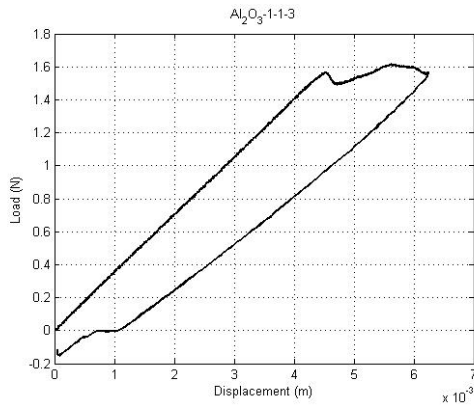


(a) Unaged  $Al_2O_3$  -1-1-2

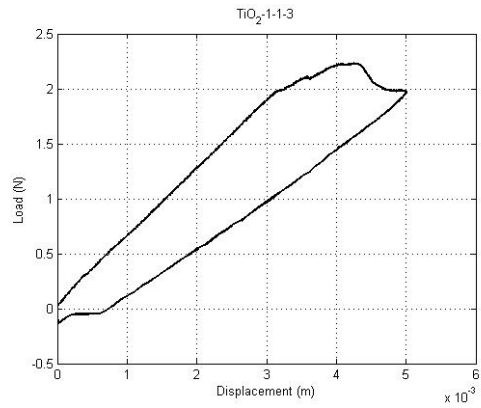


(b) Unaged  $TiO_2$  -1-1-2

**Figure B.2. Second-pull load displacement curves for sample 1/beam 1 unaged  $Al_2O_3$ -coated (left) and  $TiO_2$ -coated (right) reflectors.**

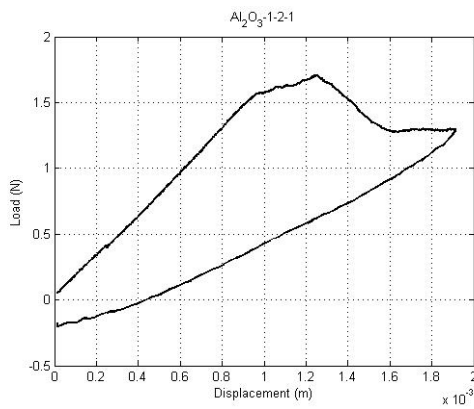


(a) Unaged  $Al_2O_3$  -1-1-3

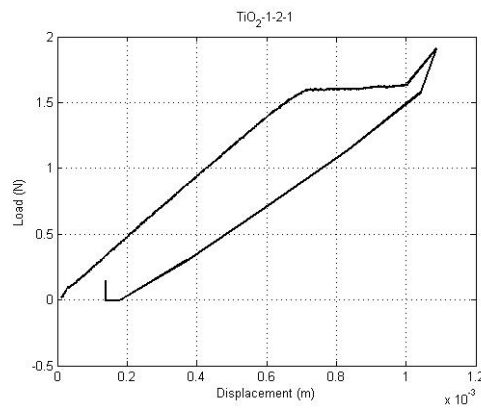


(b) Unaged  $TiO_2$  -1-1-3

**Figure B.3. Third-pull load displacement curves for sample 1/beam 1 unaged  $Al_2O_3$ -coated (left) and  $TiO_2$ -coated (right) reflectors.**

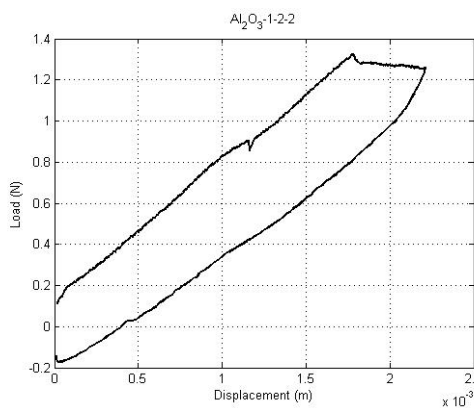


(a) Unaged  $Al_2O_3$  -1-2-1

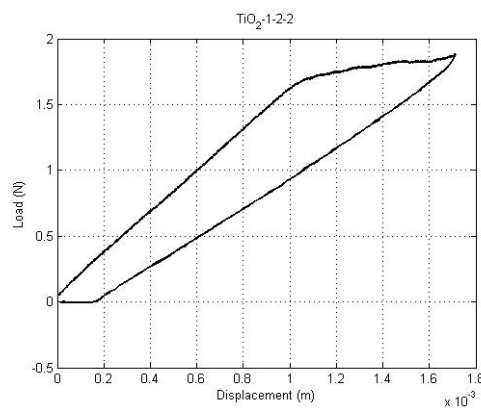


(b) Unaged  $TiO_2$  -1-2-1

**Figure B.4. First-pull load displacement curves for sample 1/beam 2 unaged  $Al_2O_3$ -coated (left) and  $TiO_2$ -coated (right) reflectors.**

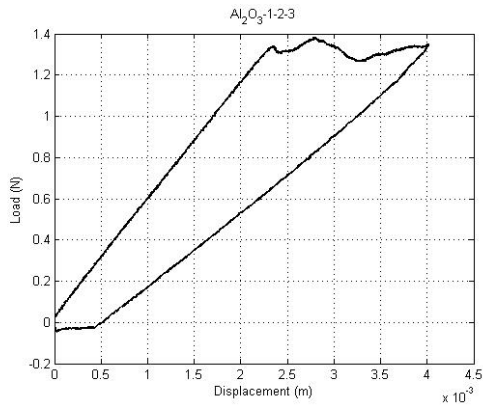


(a) Unaged  $Al_2O_3$  -1-2-2

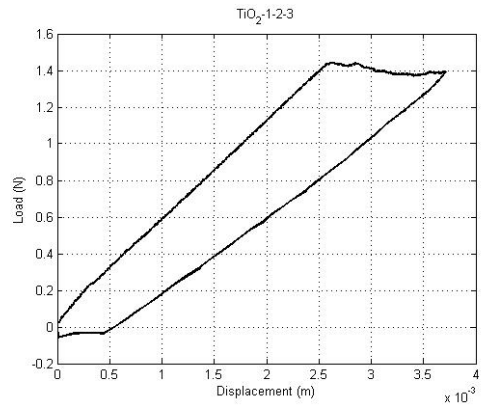


(b) Unaged  $TiO_2$  -1-2-2

**Figure B.5. Second-pull load displacement curves for sample 1/beam 2 unaged  $Al_2O_3$ -coated (left) and  $TiO_2$ -coated (right) reflectors.**

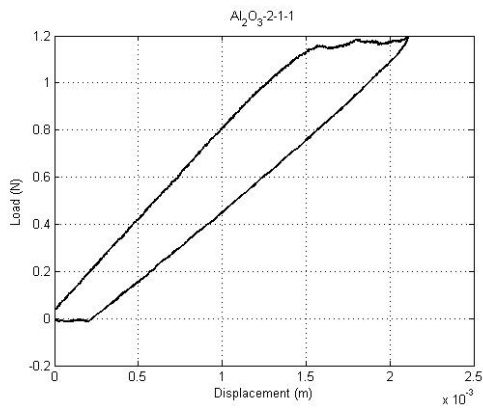


(a) Unaged  $Al_2O_3$  -1-2-3

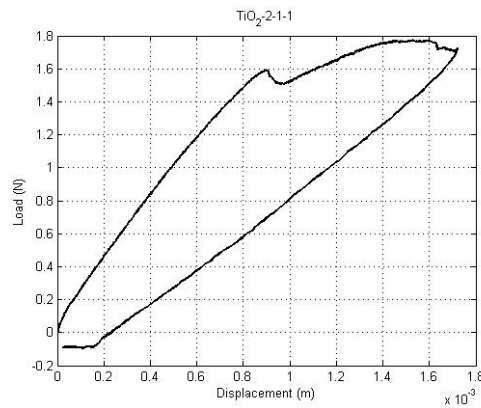


(b) Unaged  $TiO_2$  -1-2-3

**Figure B.6. Third-pull load displacement curves for sample 1/beam 2 unaged  $Al_2O_3$ -coated (left) and  $TiO_2$ -coated (right) reflectors.**

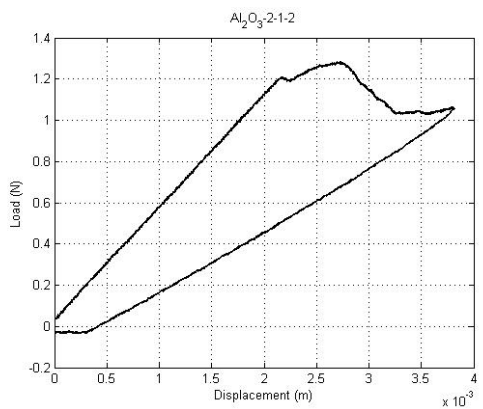


(a) Unaged  $Al_2O_3$  -2-1-1

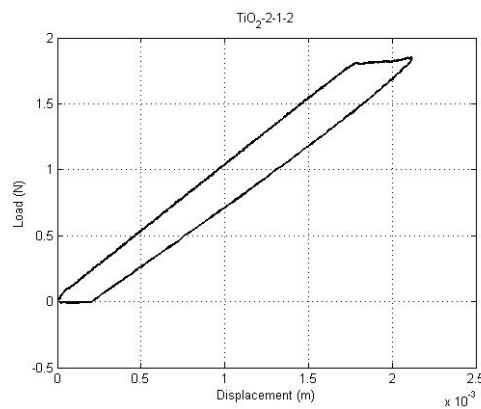


(b) Unaged  $TiO_2$  -2-1-1

**Figure B.7. First-pull load displacement curves for sample 2/beam 1 unaged  $Al_2O_3$ -coated (left) and  $TiO_2$ -coated (right) reflectors.**

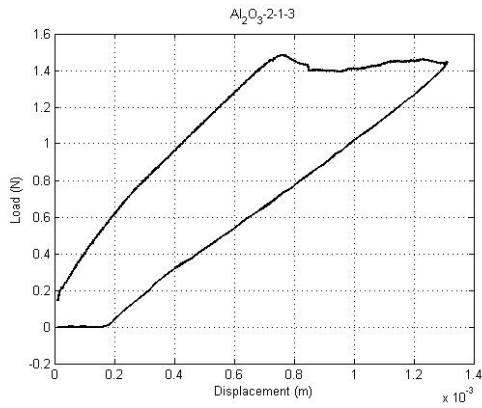


(a) Unaged  $Al_2O_3$  -2-1-2

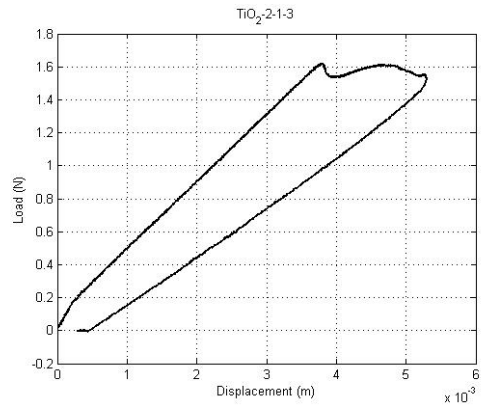


(b) Unaged  $TiO_2$  -2-1-2

**Figure B.8. Second-pull load displacement curves for sample 2/beam 1 unaged  $Al_2O_3$ -coated (left) and  $TiO_2$ -coated (right) reflectors.**

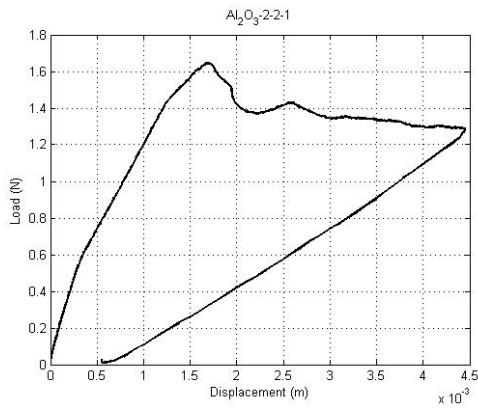


(a) Unaged  $Al_2O_3$  -2-1-3

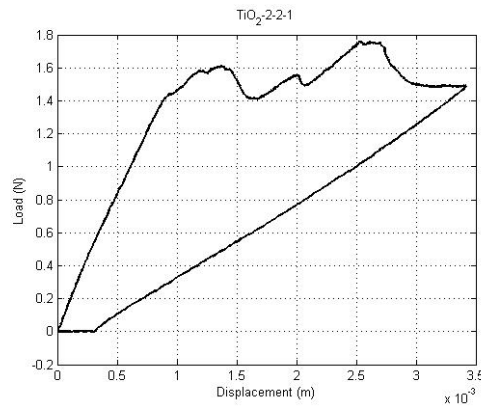


(b) Unaged  $TiO_2$  -2-1-3

**Figure B.9. Third-pull load displacement curves for sample 2/beam 1 unaged  $Al_2O_3$ -coated (left) and  $TiO_2$ -coated (right) reflectors.**

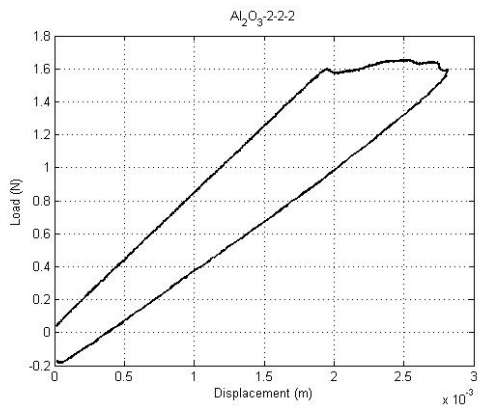


(a) Unaged  $Al_2O_3$  -2-2-1

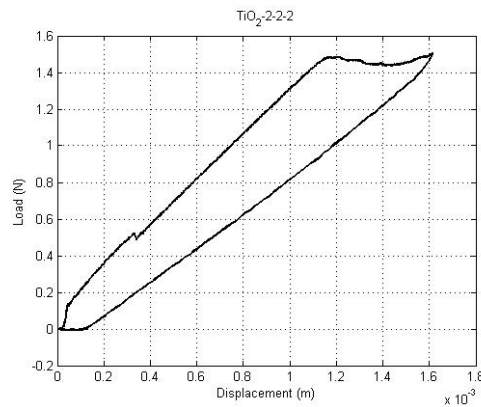


(b) Unaged  $TiO_2$  -2-2-1

**Figure B.10. First-pull load displacement curves for sample 2/beam 2 unaged  $Al_2O_3$ -coated (left) and  $TiO_2$ -coated (right) reflectors.**

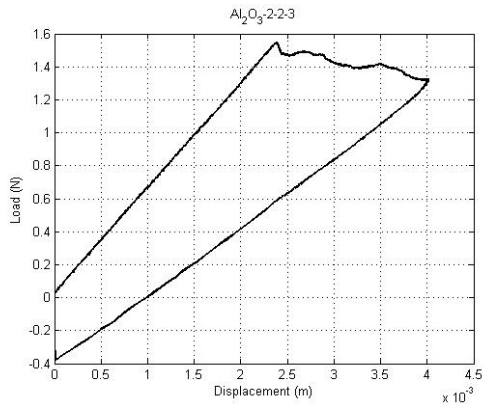


(a) Unaged  $Al_2O_3$  -2-2-2

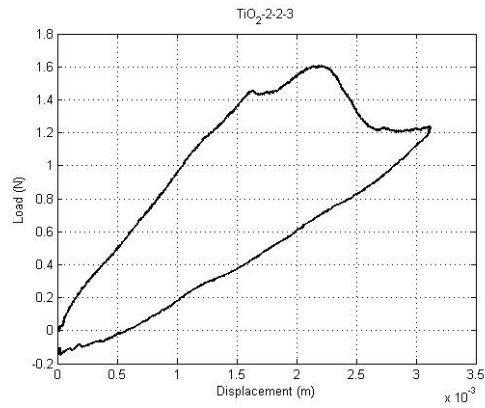


(b) Unaged  $TiO_2$  -2-2-2

**Figure B.11. Second-pull load displacement curves for sample 2/beam 2 unaged  $Al_2O_3$ -coated (left) and  $TiO_2$ -coated (right) reflectors.**

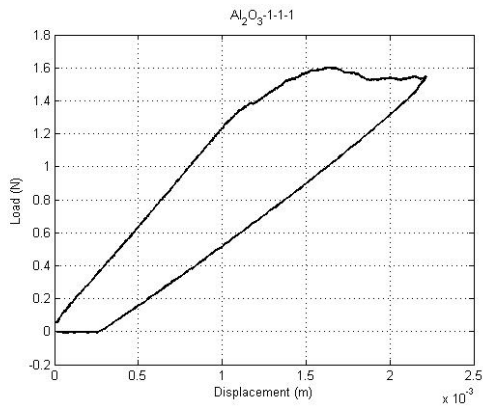


(a) Unaged  $Al_2O_3$  -2-2-3

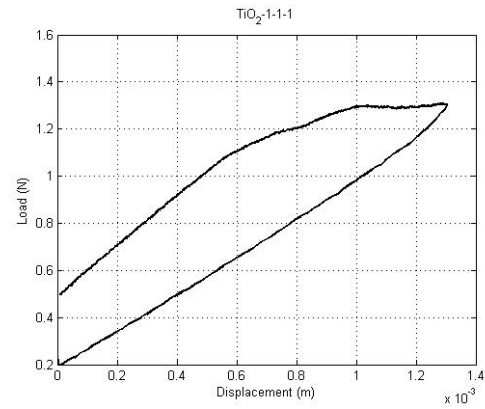


(b) Unaged  $TiO_2$  -2-2-3

**Figure B.12. Third-pull load displacement curves for sample 2/beam 2 unaged  $Al_2O_3$ -coated (left) and  $TiO_2$ -coated (right) reflectors.**

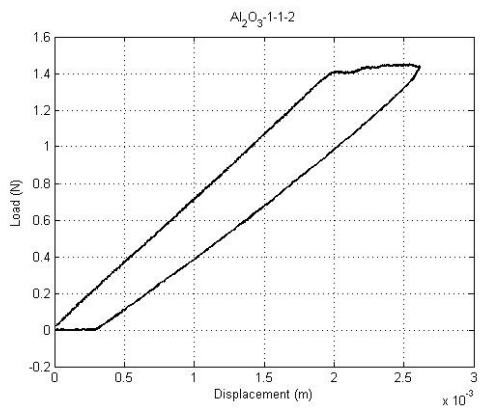


(a)  $Al_2O_3$  -1-1-1 aged for 50 hours

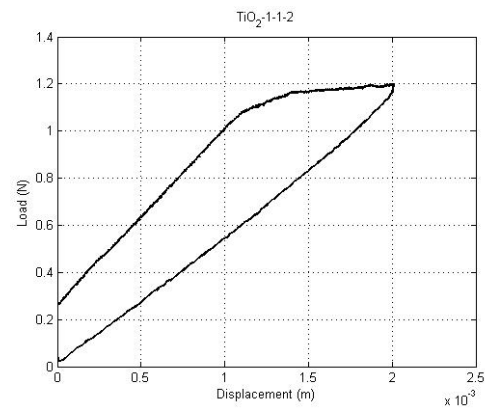


(b)  $TiO_2$  -1-1-1 aged for 50 hours

**Figure B.13. First-pull load displacement curves for sample 1/beam 1  $Al_2O_3$ -coated (left) and  $TiO_2$ -coated (right) reflectors aged 50 hours.**

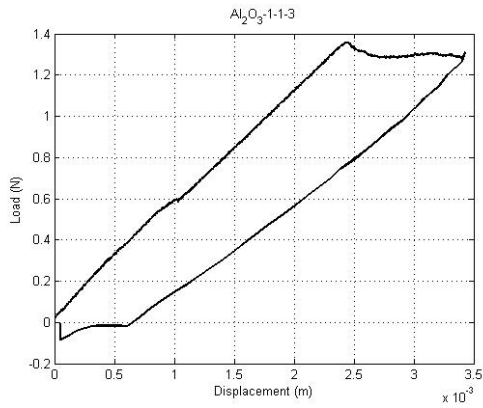


(a)  $Al_2O_3$  -1-1-2 aged for 50 hours

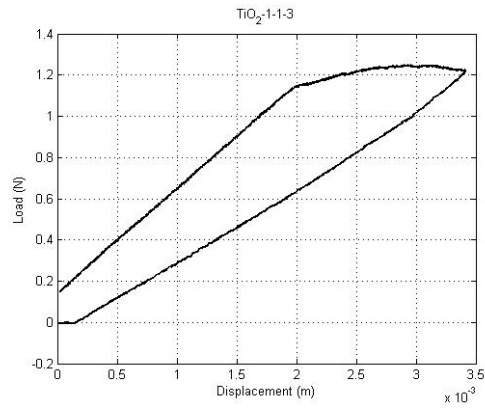


(b)  $TiO_2$  -1-1-2 aged for 50 hours

**Figure B.14. Second-pull load displacement curves for sample 1/beam 1  $Al_2O_3$ -coated (left) and  $TiO_2$ -coated (right) reflectors aged 50 hours.**

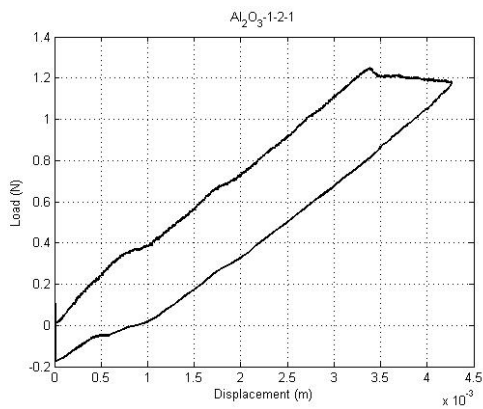


(a)  $Al_2O_3$  -1-1-3 aged for 50 hours

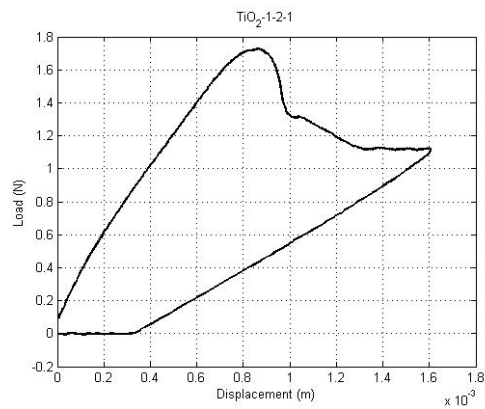


(b)  $TiO_2$  -1-1-3 aged for 50 hours

**Figure B.15. Third-pull load displacement curves for sample 1/beam 1  $Al_2O_3$ -coated (left) and  $TiO_2$ -coated (right) reflectors aged 50 hours.**

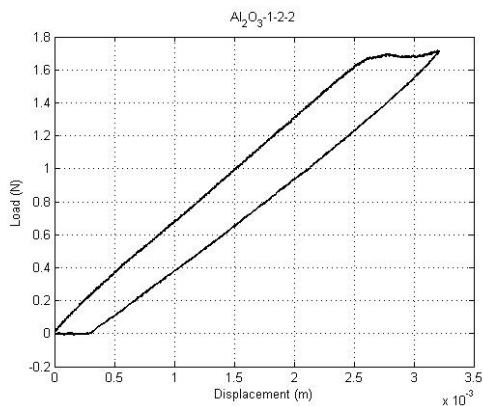


(a)  $Al_2O_3$  -1-2-1 aged for 50 hours

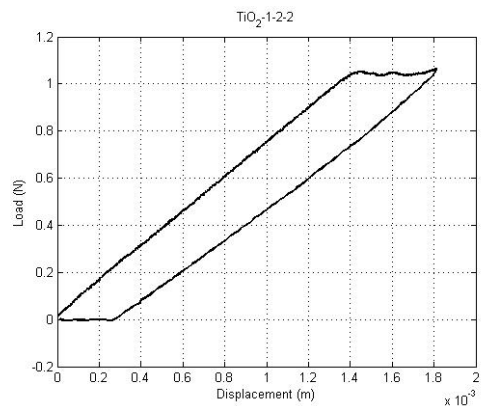


(b)  $TiO_2$  -1-2-1 aged for 50 hours

**Figure B.16. First-pull load displacement curves for sample 1/beam 2  $Al_2O_3$ -coated (left) and  $TiO_2$ -coated (right) reflectors aged 50 hours.**

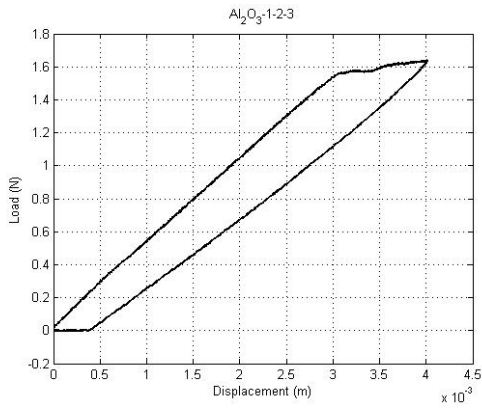


(a)  $Al_2O_3$  -1-2-2 aged for 50 hours

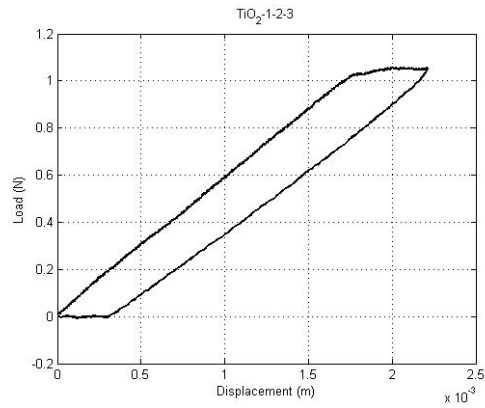


(b)  $TiO_2$  -1-2-2 aged for 50 hours

**Figure B.17. Second-pull load displacement curves for sample 1/beam 2  $Al_2O_3$ -coated (left) and  $TiO_2$ -coated (right) reflectors aged 50 hours.**

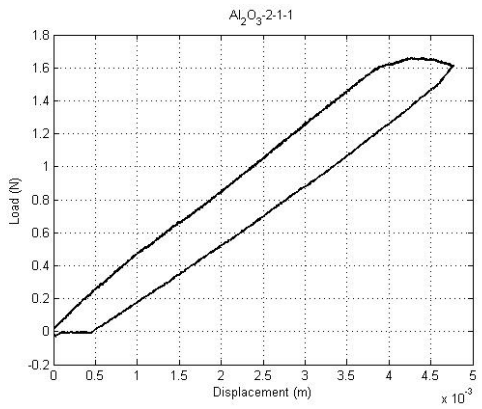


(a)  $Al_2O_3$  -1-2-3 aged for 50 hours

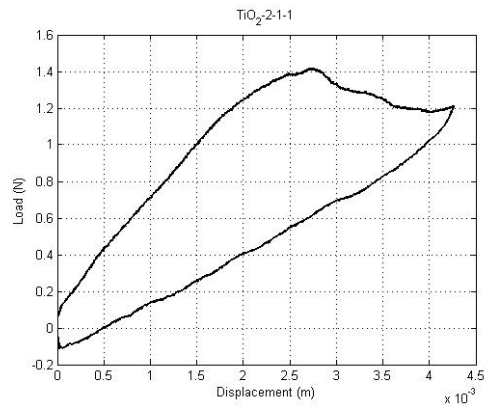


(b)  $TiO_2$  -1-2-3 aged for 50 hours

**Figure B.18. Third-pull load displacement curves for sample 1/beam 2  $Al_2O_3$ -coated (left) and  $TiO_2$ -coated (right) reflectors aged 50 hours.**

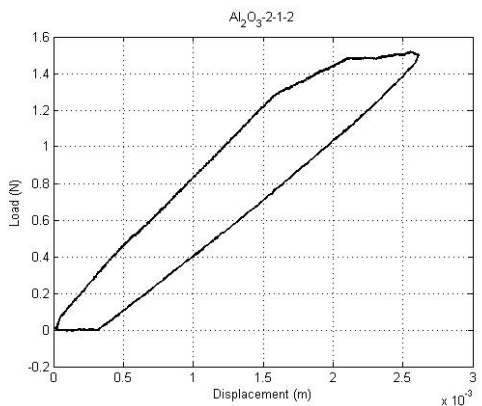


(a)  $Al_2O_3$  -2-1-1 aged for 50 hours

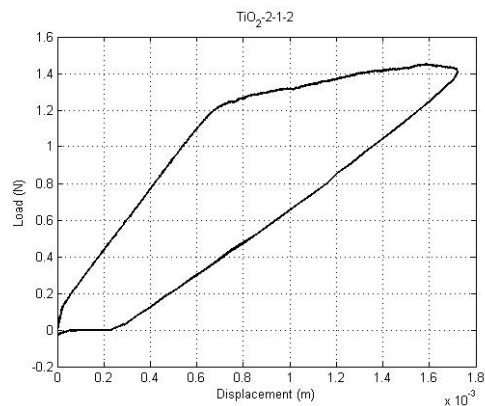


(b)  $TiO_2$  -2-1-1 aged for 50 hours

**Figure B.19. First-pull load displacement curves for sample 2/beam 1  $Al_2O_3$ -coated (left) and  $TiO_2$ -coated (right) reflectors aged 50 hours.**

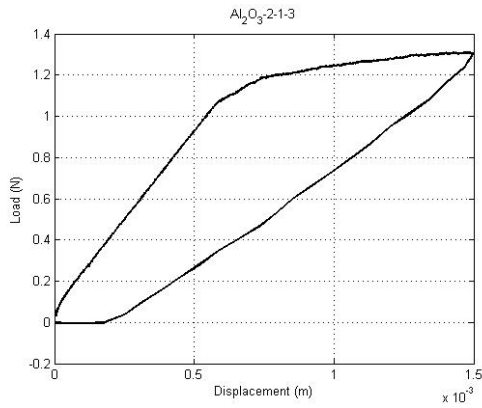


(a)  $Al_2O_3$  -2-1-2 aged for 50 hours

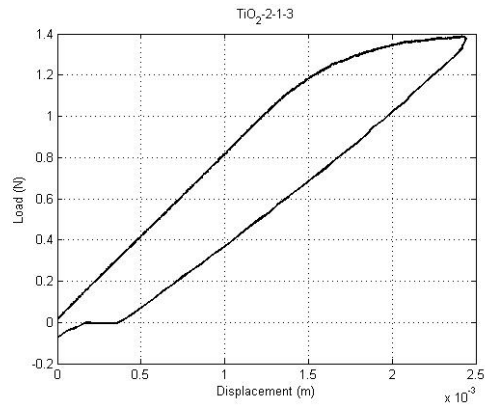


(b)  $TiO_2$  -2-1-2 aged for 50 hours

**Figure B.20. Second-pull load displacement curves for sample 2/beam 1  $Al_2O_3$ -coated (left) and  $TiO_2$ -coated (right) reflectors aged 50 hours.**

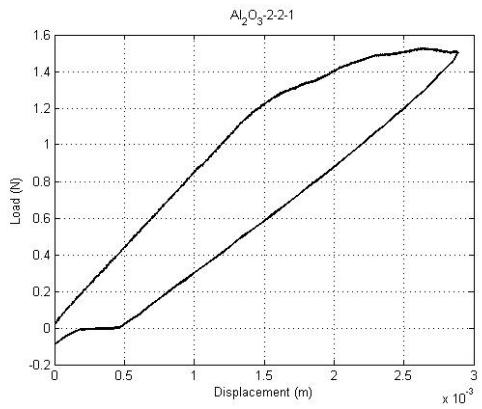


(a)  $Al_2O_3$  -2-1-3 aged for 50 hours

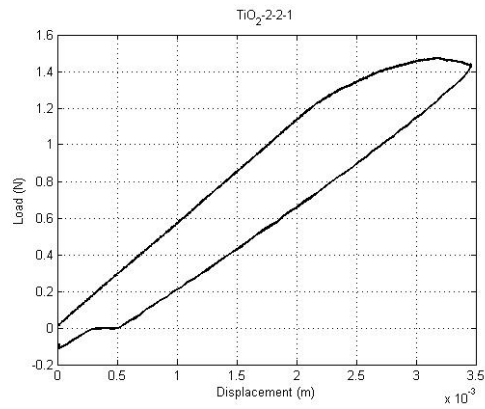


(b)  $TiO_2$  -2-1-3 aged for 50 hours

**Figure B.21. Third-pull load displacement curves for sample 2/beam 1  $Al_2O_3$ -coated (left) and  $TiO_2$ -coated (right) reflectors aged 50 hours.**

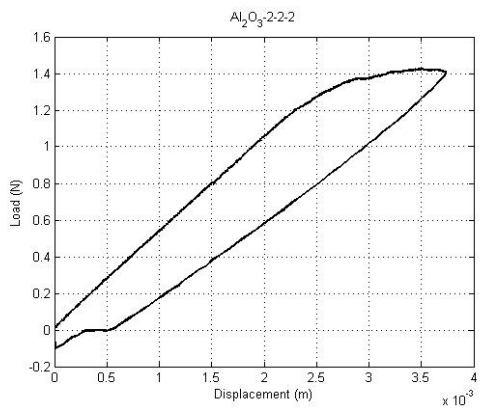


(a)  $Al_2O_3$  -2-2-1 aged for 50 hours

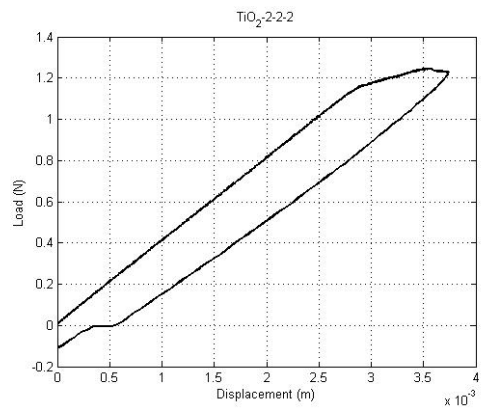


(b)  $TiO_2$  -2-2-1 aged for 50 hours

**Figure B.22. First-pull load displacement curves for sample 2/beam 2  $Al_2O_3$ -coated (left) and  $TiO_2$ -coated (right) reflectors aged 50 hours.**

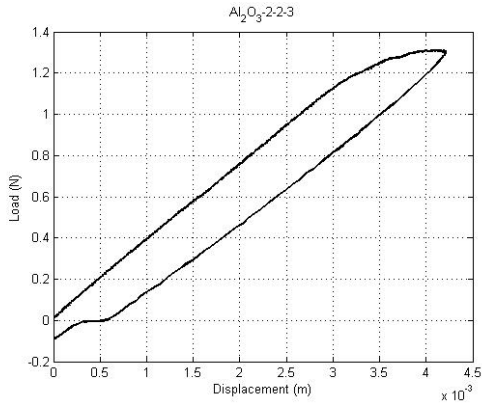


(a)  $Al_2O_3$  -2-2-2 aged for 50 hours

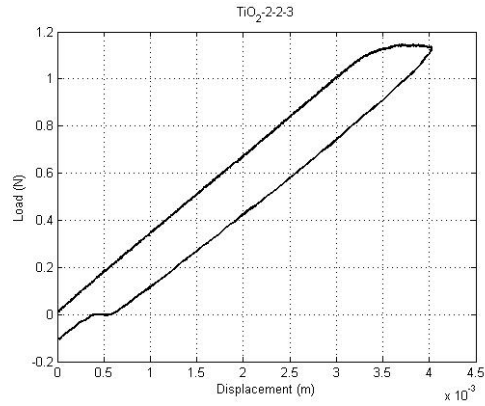


(b)  $TiO_2$  -2-2-2 aged for 50 hours

**Figure B.23. Second-pull load displacement curves for sample 2/beam 2  $Al_2O_3$ -coated (left) and  $TiO_2$ -coated (right) reflectors aged 50 hours.**

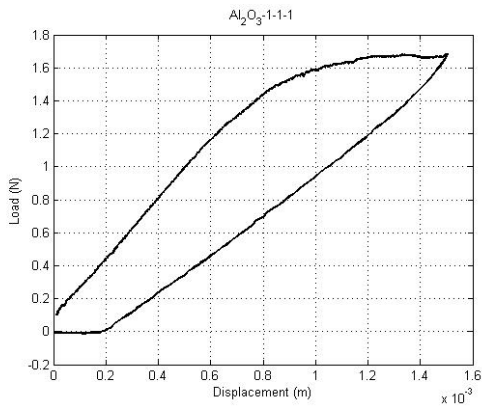


(a)  $Al_2O_3$  -2-2-3 aged for 50 hours

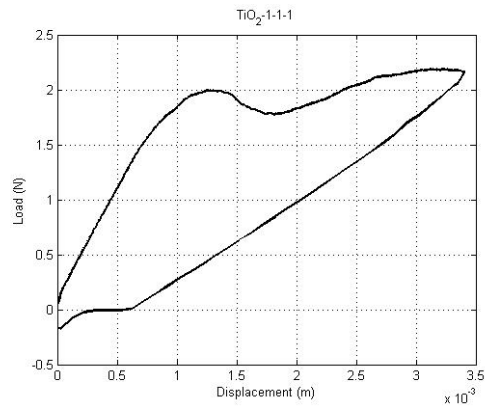


(b)  $TiO_2$  -2-2-3 aged for 50 hours

**Figure B.24. Third-pull load displacement curves for sample 2/beam 2  $Al_2O_3$ -coated (left) and  $TiO_2$ -coated (right) reflectors aged 50 hours.**

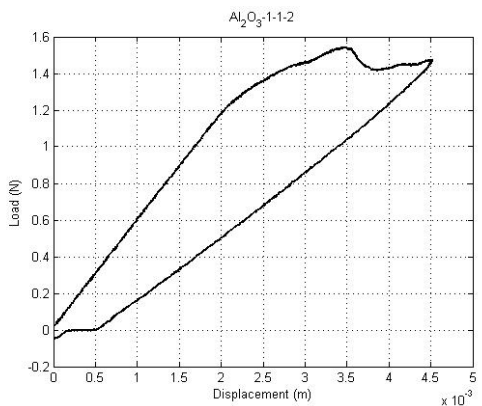


(a)  $Al_2O_3$  -1-1-1 aged for 100 hours

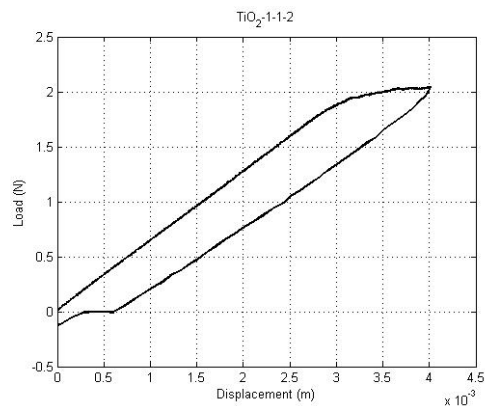


(b)  $TiO_2$  -1-1-1 aged for 100 hours

**Figure B.25. First-pull load displacement curves for sample 1/beam 1  $Al_2O_3$ -coated (left) and  $TiO_2$ -coated (right) reflectors aged 100 hours.**

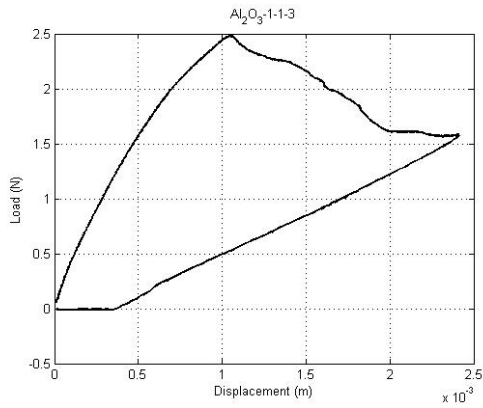


(a)  $Al_2O_3$  -1-1-2 aged for 100 hours

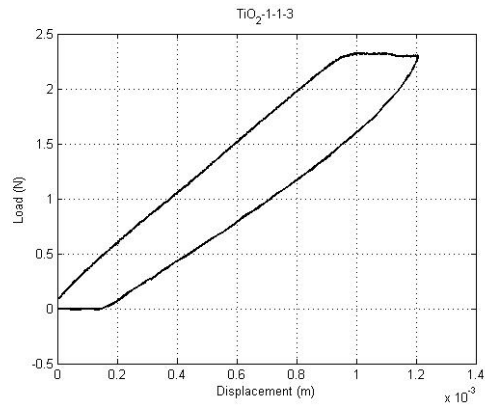


(b)  $TiO_2$  -1-1-2 aged for 100 hours

**Figure B.26. Second-pull load displacement curves for sample 1/beam 1  $Al_2O_3$ -coated (left) and  $TiO_2$ -coated (right) reflectors aged 100 hours.**

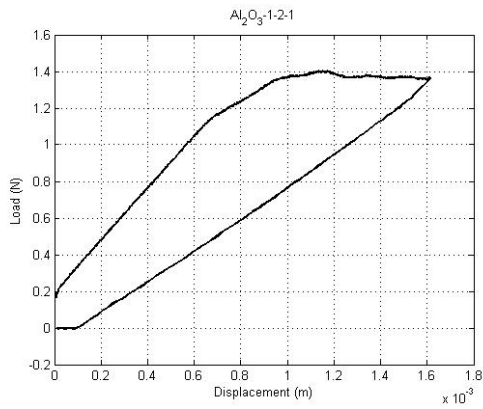


(a)  $Al_2O_3$  -1-1-3 aged for 100 hours

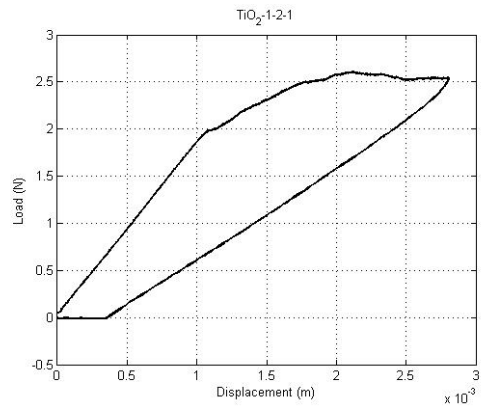


(b)  $TiO_2$  -1-1-3 aged for 100 hours

**Figure B.27. Third-pull load displacement curves for sample 1/beam 1  $Al_2O_3$ -coated (left) and  $TiO_2$ -coated (right) reflectors aged 100 hours.**

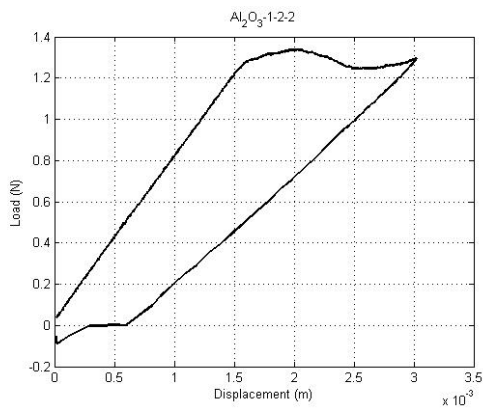


(a)  $Al_2O_3$  -1-2-1 aged for 100 hours

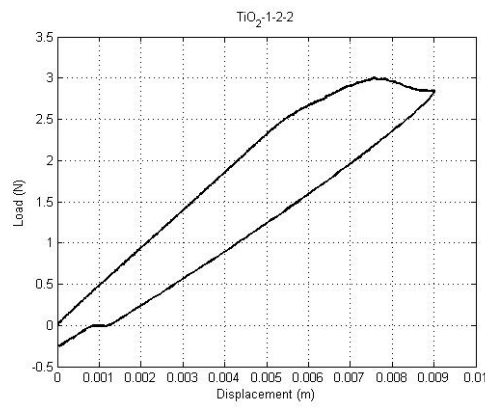


(b)  $TiO_2$  -1-2-1 aged for 100 hours

**Figure B.28. First-pull load displacement curves for sample 1/beam 2  $Al_2O_3$ -coated (left) and  $TiO_2$ -coated (right) reflectors aged 100 hours.**

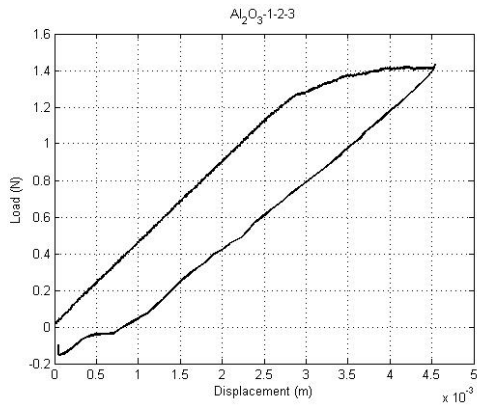


(a)  $Al_2O_3$  -1-2-2 aged for 100 hours

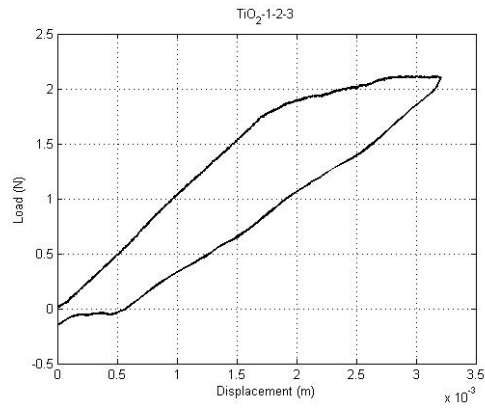


(b)  $TiO_2$  -1-2-2 aged for 100 hours

**Figure B.29. Second-pull load displacement curves for sample 1/beam 2  $Al_2O_3$ -coated (left) and  $TiO_2$ -coated (right) reflectors aged 100 hours.**

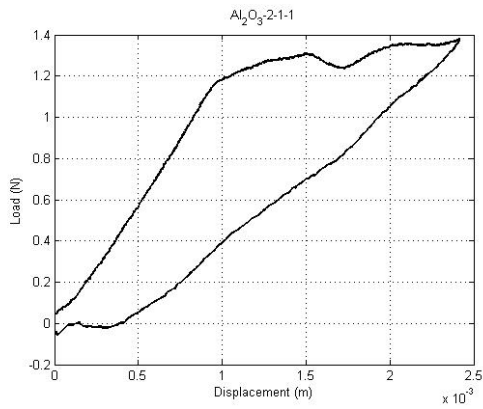


(a)  $Al_2O_3$  -1-2-2 aged for 100 hours

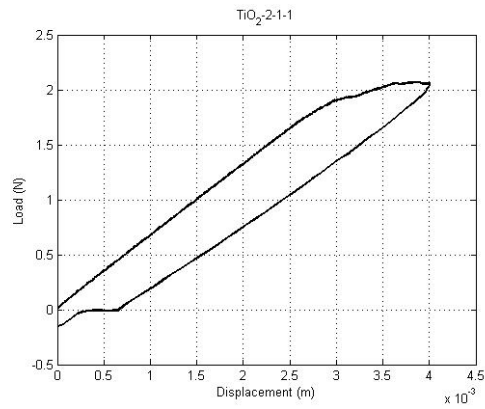


(b)  $TiO_2$  -1-2-3 aged for 100 hours

**Figure B.30. Third-pull load displacement curves for sample 1/beam 2  $Al_2O_3$ -coated (left) and  $TiO_2$ -coated (right) reflectors aged 100 hours.**

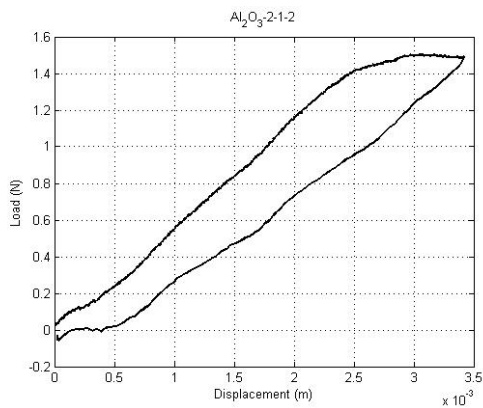


(a)  $Al_2O_3$  -2-1-1 aged for 100 hours

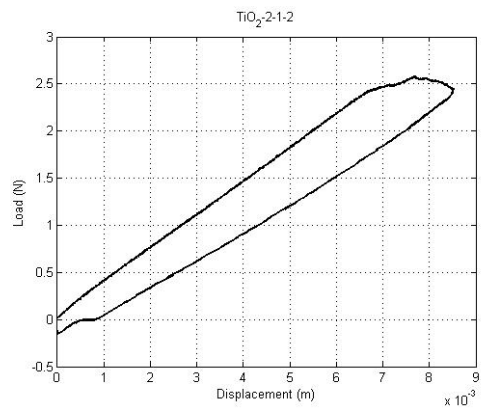


(b)  $TiO_2$  -2-1-1 aged for 100 hours

**Figure B.31. First-pull load displacement curves for sample 2/beam 1  $Al_2O_3$ -coated (left) and  $TiO_2$ -coated (right) reflectors aged 100 hours.**

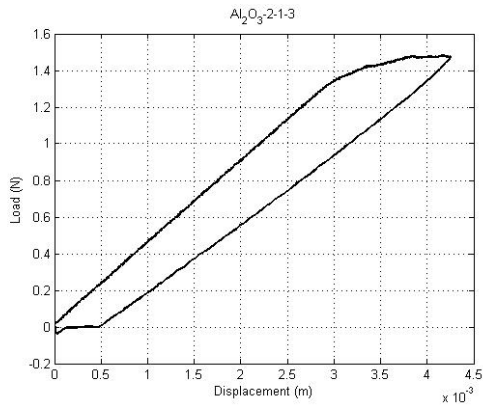


(a)  $Al_2O_3$  -2-1-2 aged for 100 hours

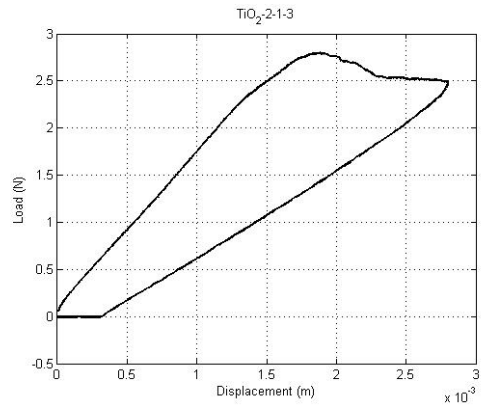


(b)  $TiO_2$  -2-1-2 aged for 100 hours

**Figure B.32. Second-pull load displacement curves for sample 2/beam 1  $Al_2O_3$ -coated (left) and  $TiO_2$ -coated (right) reflectors aged 100 hours.**

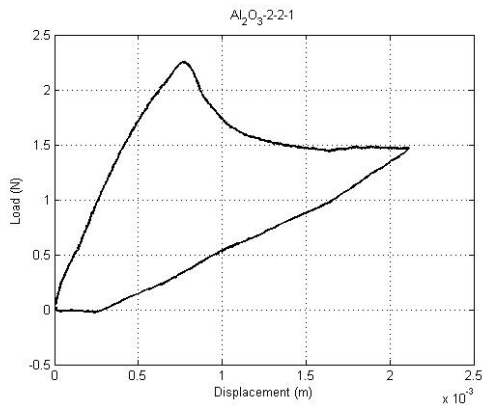


(a)  $Al_2O_3$  -2-1-3 aged for 100 hours

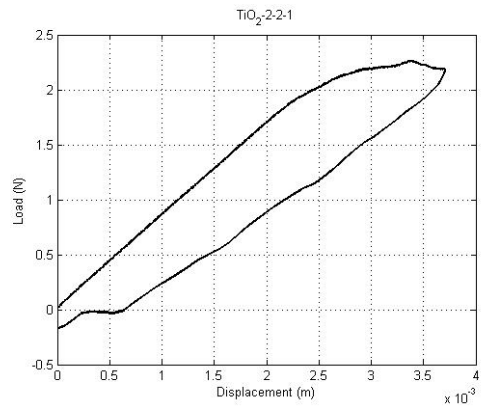


(b)  $TiO_2$  -2-1-3 aged for 100 hours

**Figure B.33. Third-pull load displacement curves for sample 2/beam 1  $Al_2O_3$ -coated (left) and  $TiO_2$ -coated (right) reflectors aged 100 hours.**

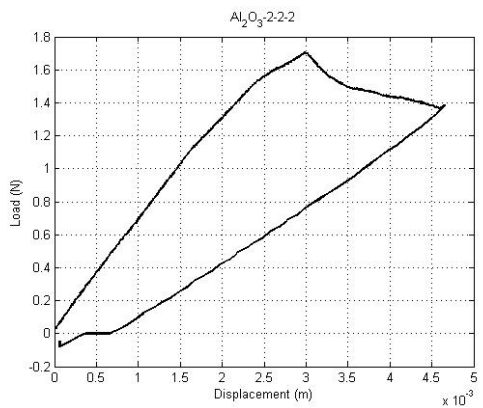


(a)  $Al_2O_3$  -2-2-1 aged for 100 hours

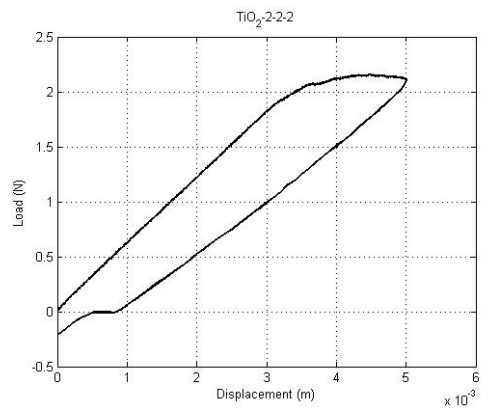


(b)  $TiO_2$  -2-2-1 aged for 100 hours

**Figure B.34. First-pull load displacement curves for sample 2/beam 2  $Al_2O_3$ -coated (left) and  $TiO_2$ -coated (right) reflectors aged 100 hours.**

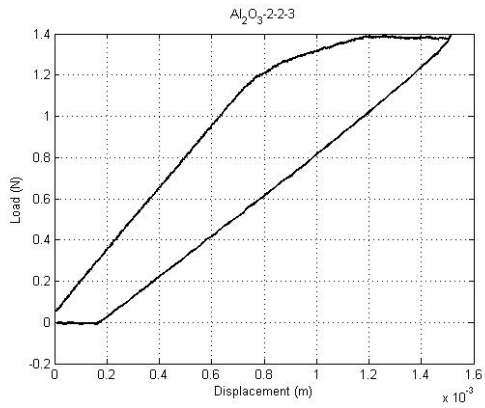


(a)  $Al_2O_3$  -2-2-2 aged for 100 hours

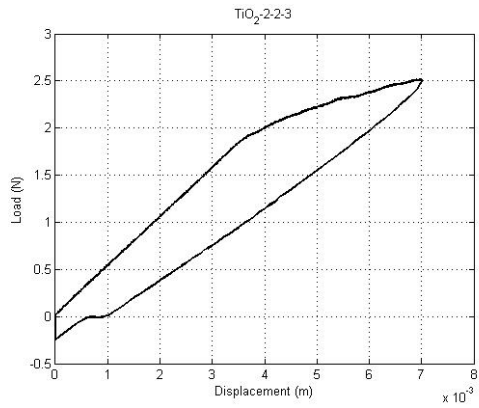


(b)  $TiO_2$  -2-2-2 aged for 100 hours

**Figure B.35. Second-pull load displacement curves for sample 2/beam 2  $Al_2O_3$ -coated (left) and  $TiO_2$ -coated (right) reflectors aged 100 hours.**



(a)  $Al_2O_3$  -2-2-3 aged for 100 hours



(b)  $TiO_2$  -2-2-3 aged for 100 hours

**Figure B.36. Third-pull load displacement curves for sample 2/beam 2  $Al_2O_3$ -coated (left) and  $TiO_2$ -coated (right) reflectors aged 100 hours.**